

DELFT UNIVERSITY OF TECHNOLOGY

**Wind Modification and Aerodynamic
Parameters: Supporting Heat Stress
Research for a Resilient Urban Environment**

ADDITIONAL THESIS

Author:

M. O'Hanrahan (5627796)

September 16, 2023



Abstract

Understanding wind profiles in urban areas is vital for a range of applications including urban planning and environmental science. This study aims to characterize the modification of wind profiles in The Heat Square through anemometer observations, focusing on the influence of building morphology. Previous studies have endorsed methodologies that consider building height variability, but our results suggest that rule-of-thumb morphometric methods based on average building height offer closer anemometric estimates in this specific urban setting. Unfortunately, the lack of inertial sublayer (ISL) wind speed measurements constrains the generalizability of our findings. Additionally, sub-optimal anemometer installation height poses another limitation to the study. Despite these constraints, the results should serve as reasonable estimates for modeling efforts concerning heat flux and heat stress. The study strongly recommends further research to address existing limitations, aiming to generate more reliable field estimates, particularly for The Heat Square and The Green Village.

I Acronyms

Acronym	Translation
ABL	Atmospheric Boundary Layer
ASL	Atmospheric Surface Layer
ISL	Inertial Sub-layer
ME	Mean Error
MOST	Monin-Obukhov Similarity Theory
PET	Physiological Equivalent Temperature
RSL	Roughness Sub-layer
SEB	Surface Energy Balance
THS	The Heat Square (central to the green village)
TGV	The Green Village
TU	Technische Universiteit (Delft)
UBL	Urban Boundary Layer
UCL	Urban Canopy Layer
UHI	Urban Heat Island
UMEP	Urban Multi-scale Environmental Predictor
TKE	Turbulent Kinetic Energy
Ri_f	Richardson number
RI_b	Richardson-bulk method

II Variables, Constants and Symbology

Symbol	Full Name	Units
Q^*	Surface Net All Wave Radiation	W m^{-2}
H	Sensible Heat Flux	W m^{-2}
$L_v E$	Latent Heat Flux	W m^{-2}
G	Ground Heat Flux	W m^{-2}
z_d	Zero-Plane Displacement Height	m
z_0	Aerodynamic Roughness Length	m
$\bar{\theta}_v$	Mean Virtual Potential Temperature	K
u^*	Friction Velocity	m/s
κ	von Kármán Constant	Dimensionless
g	Acceleration Due to Gravity	m/s^2
θ_*	Temperature Scale	K
L	Obukhov Length	m
$w'\theta'$	Surface Virtual Potential Heat Flux	W m^{-2}
$z_{0,h}$	Roughness Length for Heat	m
z_1	Lower Measurement Height	m
h_c	Average Height of the Canopy	m
$\phi_{m,h,e}$	Universal Function for MOST	Dimensionless
Ri_f	Richardson Number	Dimensionless
TKE	Turbulent Kinetic Energy	m^2/s^2
$\Delta\bar{\theta}_v$	Change in Virtual Potential Temperature	K
Δz	Height Difference Between Two Wind Speed Sensors	m
$\Delta\bar{u}$	Difference Between the Two Temporally Averaged Wind Speeds	m/s
RI_b	Richardson-Bulk Method	Dimensionless
H_{av}	Average Roughness Element Height	m
α, β	Coefficients in RT Methodology	Dimensionless
λ_p	Plan Area Index	Dimensionless
λ_f	Frontal Area Index	Dimensionless
C_{Db}	Building Drag Coefficient	Dimensionless
σ_H	Standard Deviation of Roughness Element Heights	m
A_f^*	Unsheltered Frontal Area of Building	m^2
A_T	Total Area Under Consideration	m^2
H_{max}	Maximum Roughness Element Height	m
X	Building Height Above Average, Relative to H_{max}	Dimensionless
a, b, c	Coefficients in Kan z_d Methodology	Dimensionless
a_1, b_1, c_1	Coefficients in Kan z_0 Methodology	Dimensionless
Y	Factor Allowing for Homogeneous Arrays in Kan Method	Dimensionless

Contents

I	Acronyms	ii
II	Variables, Constants and Symbology	iii
1	Introduction	1
2	Research Objectives	5
2.a	Knowledge Gap	5
2.b	Research Questions	5
3	Background	6
4	Materials and Methods	9
4.a	Software	9
4.b	Data	9
4.c	Location	10
4.d	Additional Installation	10
4.e	Methodology	11
4.f	Morphometric Estimation	14
5	Results and Discussion	18
5.a	Exploratory Analysis	19
5.b	Aerodynamic Parameter Estimation	23
5.c	Data Issues	23
5.d	Spatial Variability Within The Heat Square	24
5.e	Anisotropic Parameter Variability	27
5.f	Profile Extrapolation Comparison	29
6	Discussion	30
6.a	Modification and Morphology	30
6.b	Parameter Estimations	30
6.c	Aerodynamic Roughness Length	30
6.d	Zero-Plane Displacement	31
7	Conclusions and Recommendations	32
A	Code and Data Repositories	33
B	Additional Equations	33
C	Additional Tables	33
D	Extra Results	35
D.a	Exploratory Analysis	35



Figure 1: Location of The Heat Square within The Green Village and Anemometer Locations.

1 Introduction

The human population increasingly inhabits urban areas. Rural to-urban population migration is The trend towards urbanization is set to continue unabated, with global projections indicating that the proportion of the population living in urban areas will rise from 54% in 2016 to 66% by 2050 (Kousis et al., 2021; Jiang and O'Neill, 2017). In the face of a changing climate, enhancing the resilience of urban design to environmental challenges is not only a matter of public health and well-being but also an imperative for policymakers and governing organizations. Although heat stress has been identified as a significant public health risk affecting both the young and the elderly, the scientific community is still working to fully understand heat dynamics in urban settings and formulate effective mitigation strategies (Ye and Niyogi, 2022).

To address these challenges, The Green Village (TGV) at Technische Universiteit (TU) Delft is at the forefront of research into resilient urban design. TGV is engaged in implementing and rigorously monitoring various interventions aimed at bridging existing knowledge gaps and paving the way for more climate-resilient urban environments (Pino, 2021a,b).

The Heat Square (THS), a central feature of The Green Village, serves as a real-world testing ground for urban heat stress research (refer to figures 1, 3). Recently revamped in January 2023, this "*living laboratory*" incorporates carefully planned modifications in morphology, materials, and vegetation, all equipped with specialised monitoring instruments. The goal is to explore effective

methods for mitigating heat stress in urban public areas.

Heat stress poses a significant issue for city-dwellers, largely due to the historical urban design practices that have favoured "grey" spaces over green and blue spaces (i.e., areas with vegetation and water features). Such an imbalance has led to cities filled with materials like concrete and asphalt, with higher heat retention and lower permeability. These "grey" areas not only contribute to localised heat stress but also have a cumulative effect at the city level, intensifying the "Urban Heat Island" (UHI) phenomenon (Shahfahad et al., 2021; Ayub et al., 2021).

Furthermore, the urban atmospheric conditions are notably complex, with irregular airflows and pollution that can exacerbate heat stress. Polluted air can further increase thermal energy, complicating the challenges associated with heat in an urban environment.

The complexity of urban surfaces plays a significant role in horizontal heat and momentum advection. The turbulent exchange of energy, mass, and momentum in the atmosphere is critical for dissipation these variables (Coceal and Belcher, 2004). Specifically, the atmospheric boundary layer (ABL), the troposphere's lowermost section, is turbulent, influenced by diurnal heating and wind flow (Wyngaard, 2010).

Within the ABL, the atmospheric surface layer (ASL), which constitutes approximately the lowest 10% of the ABL, is a focal point for turbulence generation or suppression. This is driven by the diurnal patterns of net radiation, resulting in steep gradients of various fluxes. Surface-induced heating contributes to ABL destabilisation by stimulating buoyancy and vertical mixing. This process is intrinsically tied to the vertical gradients of scalar quantities, which play a crucial role in the dissipation of heat and mass. Thus, the effective dispersal of heat and momentum is governed mainly by these vertical scalar gradients.

The logarithmic wind law after Tennekes (1973) describes the vertical profile of momentum in a neutral atmosphere:

$$\bar{u}(z) = \frac{u_*}{\kappa} \ln\left(\frac{z - z_d}{z_0}\right) \quad (1)$$

Estimating the aerodynamic parameters z_0 and z_d is a pivotal challenge in urban boundary layer (UBL) research due to the highly heterogeneous and complex surface morphologies encountered. These parameters are integral to the accurate computation of momentum and heat fluxes, as they modulate wind shear at the surface (Kent et al., 2017; Barlow, 2014; Roth, 2000).

The phenomenon of surface irregularities, termed "roughness elements," can manifest in both natural forms like vegetation or as man-made features in urban settings. Within the atmospheric boundary layer (ABL), there exists a specialised stratum known as the *roughness sub-layer* (RSL). The RSL is characterised by highly varied flow dynamics influenced by the local geometry of the surface. These roughness elements—whether they are natural formations like trees or artificial ones like buildings—perturb the local airflow, causing wake effects that modify horizontal flows around and above their structures.

The vertical extent of the RSL is generally between two and five times the average height of the

roughness elements H_{av} , as schematically outlined in figure 2 (Barlow, 2014). The layer starting from the surface up to H_{av} is termed the *urban canopy layer* (Oke and Cleugh, 1987; Christen, 2005). Turbulence generated by these roughness elements is a key factor affecting the dispersion of heat and pollutants in urban spaces. Understanding the relationship between surface roughness and the transport of momentum and heat is therefore crucial for UBL studies.

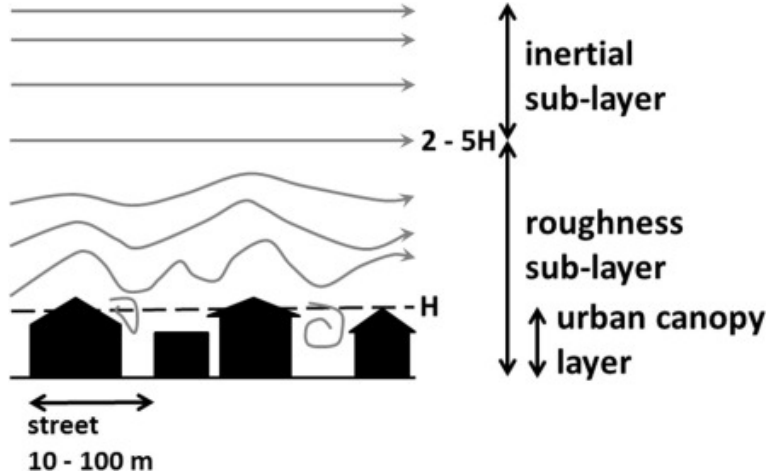


Figure 2: A schematic subdivision of the ASL above urbanised landcover showing the urban canopy layer (UCL) roughness sub-layer (RSL) and the inertial sub-layer (ISL) from Barlow (2014)

Estimation of aerodynamic parameters in the urban environment traditionally employs three main methodologies: (i) reference-based, (ii) anemometric (micrometeorological), and (iii) morphometric. Reference-based methods primarily leverage aerial photography and roughness element data—both height and density—to provide initial estimates (Grimmond and Oke, 1999; Kent et al., 2017). On the other hand, morphometric and anemometric methodologies take into account the specific surface features of the study area, offering flexibility in dealing with varying wind speed, direction, or atmospheric stability.

Morphometric approaches derive their estimates from the collective geometry and porosity of upwind roughness elements. Grimmond and Oke (1999) noted in a review that the estimation of aerodynamic parameters is fraught with uncertainties. This is largely due to the interaction between wind direction and the geometry of buildings, resulting in a wide range of possible estimates. To handle these issues, indices characterizing upwind areas are often developed, as discussed in the methodologies section. Kent et al. (2017) compared several morphometric methodologies using the UMEP tool and found that although morphometric estimates often differ from anemometric ones, they tend to be more consistent when extrapolating wind profiles up to $200m$.

In this study, we utilize both morphometric and anemometric methods to estimate the aerodynamic parameters of The Heat Square (THS) situated in The Green Village. A crucial question centers on the reliability and variability of morphometric methods, especially given their potential advantages in cost and reproducibility over traditional methods. Particularly, we aim to investigate these aspects over a small spatial footprint of approximately $20m$. The primary goal is to conduct an inter-method comparison within the area of THS to scrutinize spatial variability and method sen-

sitivities. The outcome of this study aims not only to offer a range of parameter estimates specific to THS but also to shed light on the associated uncertainties and sensitivities. General wind flow characteristics within THS are also analyzed to inform future studies and recommendations.

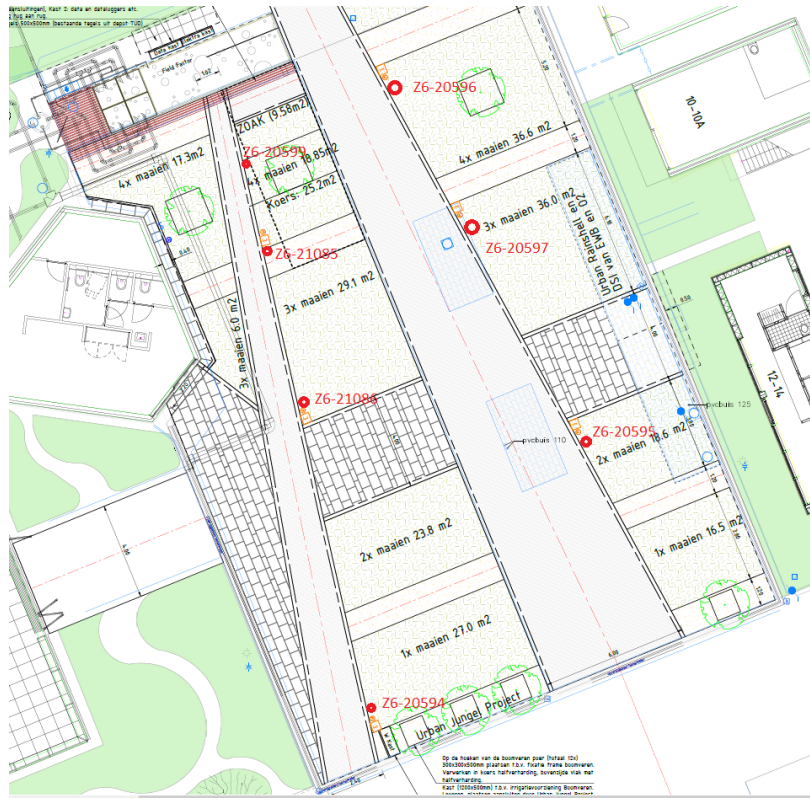


Figure 3: Locations of monitoring stations with naming convention "z6-XXXXX" marked in red within the context of The Heat Square.

2 Research Objectives

2.a Knowledge Gap

As of the time of writing, The Green Village has yet to conduct comprehensive studies on estimating aerodynamic parameters, such as roughness and displacement heights, across The Heat Square. This gap in knowledge is a critical impediment to accurately evaluating heat stress and the effectiveness of various mitigation strategies. Moreover, the characteristics of wind flow within the area remain poorly understood. Addressing these gaps is essential for any future work on heat flux modelling and small-scale wind studies within The Green Village. This paper aims to fill these knowledge gaps and serve as a foundational reference for such future research.

2.b Research Questions

1. *'What are the general characteristics of wind modification across The Heat Square in The Green Village?'*
2. *'What differences are apparent between morphometric and anemometric measures of roughness and displacement in the heat square?'*
3. *'What methodology produces the parameters that result in less error extrapolating wind profiles?'*

3 Background

The heat energy felt at the surface results primarily from solar radiation interacting with the Earth’s surface and atmosphere. The energy balance of the surface is represented in equation 2 whereby the available energy, surface net all wave radiation (Q^*), at the surface that isn’t absorbed by the ground (G) is equivalent to the energy available for the turbulent sensible heat flux (H) and turbulent latent heat flux ($L_v E$) (Oke and Cleugh, 1987) (units of Wm^{-2}). The surface energy balance (SEB) is presented below in equation 2:

$$Q^* = H + L_v E + G \quad (2)$$

Sensible heat (H) is the heat energy contained in the air and is the portion of heat energy that the observer feels in the absence of the phase change in water. The goal of heat-resilient urban design to improve thermal comfort for pedestrians in urban public spaces. Modification of surface composition by urbanisation (i.e. paving of soil or removal vegetation) increases the ratio of H to $L_v E$ (the Bowen ratio), where water is less available for those phase changes to occur Christen (2005).

For the logarithmic wind law formula, both the zero-plane displacement height (z_d) and the roughness length (z_0) are crucial for determining the momentum flux near the surface. When calculating turbulent fluxes of momentum, heat, or other scalars, the displacement height plays a role in providing a more accurate estimate of the gradients involved. This is important because gradients drive the fluxes; inaccurate representation of the wind or temperature profile can lead to errors in flux estimation (Moene and van Dam, 2014)..

For example, in an urban environment with tall buildings, the displacement height can be significant and not accounting for it may lead to underestimates of the momentum and heat fluxes at street level, which can have consequences for air quality and thermal comfort assessments.

Zero plane displacement (z_d) is introduced in the case of sufficiently dense roughness elements such that the average canopy height in the locality is accounted for. It can be interpreted as the height at which drag acts on canopy elements, meaning that the wind profile is described by similarity theory at this altitude. From a fluid mechanics perspective z_d is equivalent to the displacement thickness Bruin and Moore (1985).

The roughness length (z_0) essentially describes the height at which the surface wind speed would be zero if the wind speed’s vertical profile followed a logarithmic function. It is related to the friction velocity (u_*), and simpler models propose a direct proportionality between z_0 and u_*^2 (Charnock, 1955). In low to medium height and density urban settings like the one being studied, z_0 is expected to fall within a range of 0.3 to 1.5 meters (Grimmond and Oke, 1999). First-order estimates of z_d are typically approached by the rule of thumb (RT) expression $\frac{2}{3}h_c$ with h_c being the average height of the canopy and z_0/h_c on the order of 0.1. In practice, z_d in a dense urban setting can be on the order of 8 – 10m (Grimmond and Oke, 1999).

The link between heat and momentum arises with Monin-Obukhov similarity theory (MOST) Monin and Obukhov (1954). Similarity theory assumes similarity between two flows by matching the vertical profiles of mean wind speed, temperature, and scalar concentrations to their respective surface fluxes by introducing dimensionless gradients. This allows for the study of atmospheric flux-gradient relationships for scalars relating to vertical observations of heat and momentum. MOST relates dimensionless gradients to universal function $\phi_{m,h,e}$ of $\frac{z}{L}$, where L is the Obukhov length, a

measure of thermal stability in the boundary layer.

$$L = -\frac{\overline{\theta_v} u_*^3}{\kappa g \overline{w'\theta'}} s = \frac{\overline{\theta_v} u_*^2}{\kappa g \theta_*} \quad (3)$$

The Monin-Obukhov length L (units: m), is a key parameter in MOST. The Monin-Obukhov length is a measure of the height above the surface up to which buoyant forces are important in generating turbulence, compared to shear forces from the mean flow. $\overline{\theta_v}$ is the mean virtual potential temperature (units: K). Virtual potential temperature accounts for the effects of both moisture and temperature on the air density. u_* is the friction velocity, a parameter representing the shear stress at the surface and quantifying the momentum transferred from the atmosphere to the surface (units: m/s). κ is the von Kármán constant, a dimensionless constant that is approximately equal to 0.4. g is the acceleration due to gravity (units: m/s²). $\overline{w'\theta'}$ is the the surface virtual potential heat flux. θ_* is the temperature scale, defined by $\theta_* = -\frac{\overline{w'\theta'}}{u_*}$ (units: K). If L is negative the atmosphere is unstable, whereas positive values indicate a stable atmosphere.

In the RSL if we desire to compute fluxes, heat for example, using vertical gradients of momentum, then we can iteratively solve for that flux in atmospheric scalars. With observations originating from a single level, i.e. moving the lower (z_1) reading to zero at the surface allows for an instrumentally simple and appealing methodology for flux calculation but implies division by zero (appendix additional equation 24). To overcome this issue the aerodynamic roughness length parameter (z_0 , or $z_{0,m}$ indicating momentum) is created with the physical interpretation being the height above the surface at which the surface value of the scalar occurs. The roughness length for heat ($Z_{0,h}$) is closely related but not the same because the momentum exchange is caused by pressure forces and not molecular diffusion, as in the case of heat or temperature. The temperature profile, therefore, requires a further extrapolation than the wind profile toward the surface to coincide with the surface temperature



Figure 4: The Heat Square at TU Delft looking North with anemometers visible secured to metal poles. The closest station to the observer in the image is z6-21086 and z6-20596 is visible in the middle distance.

4 Materials and Methods

Primarily focused on wind modification and aerodynamic parameter estimation, we rely upon GIS and sonic anemometer (sonic wind and temperature) measurements to analyse the urban wind field, generate anemometric-derived parameters, and compare those to morphometric estimations.

4.a Software

Aside from those calculated using QGIS with the UMEP plugin morphometric algorithms described in 4.f, numerical analysis is accomplished using custom scripting in Python with the packages Pandas, Matplotlib, Numpy and Scipy. Plotting is similarly accomplished using QGIS in-built layout manager or Matplotlib and Geopandas. A GitHub repository with data processing and analysis code is provided in the appendix section A. Data links are also provided for the GIS project and UMEP outputs.

QGIS is an open-source geographic information system mapping software that enables interactive access to spatial data and data management capabilities. UMEP is an open-source tool developed by Lindberg et al. (2018) at Reading University, available as a QGIS plugin. The Python-based tool is multi-functional and multi-scale for environmental prediction in the urban setting. We use this tool within the QGIS GUI (graphical user interface) to acquire morphometric calculations of aerodynamic parameters across The Heat Square.

The inputs for UMEP are digital elevation and digital surface models (DEM, DSM) using the 0.5m resolution AHN Nederland (2023). The software can provide estimates that are both isotropic (all directions) and anisotropic (direction-dependent). The outputs are generated into text files that are readable in Python for analysis.

4.b Data

The Green Village data processed herein are property of The Green Village and can be made available to those with the requisite permissions. Open data, such as those available via DAVIS weather stations at TU Delft are openly provided in the repository (Delft, 2023). Other data relied upon is derived from the Dutch government, the Actueel Hoogtebestand Nederland (AHN) digital elevation model (DEM) and digital surface models (DSM) provided at a resolution of 0.5m (Nederland, 2023). This data source, funded by the Dutch Government, collects laser altimetry from aircraft and presents the data for download in the public domain.

The benefit of sonic anemometers over cup anemometers is the sampling frequency. The ATMOS-22 sonic anemometers provide 15-minute average scalar measurements for temperature and two-dimensional wind components, namely wind direction ($^{\circ}$) and wind speed (m/s) relating to temperature readings and gust speed. The 15-minute average is a standard practice whereby time-averaged windows longer than 30 minutes or more become increasingly affected by diurnal variations while also being less susceptible to noise.

The available stations have many additional variables for the same period, recording soil heat and moisture fluxes at varied depths. A summary of variables, coverage and frequency have been

included in the appendix data. See tables 6 to 9.

4.c Location

Generally, The Green Village is located on the TU Delft Campus in Delft, in the South of The Netherlands. The surrounding area is a mix of residential, educational, sports and utility buildings. The study area's northwest (NW) and southeast (SE) are open vegetated areas. Moderately mature trees exist to the southwest. Context on a neighborhood scale is best visualised in 9 further discussion of roughness elements and building morphology are discussed in section 5.a.3 where roughness elements in the morphometric search radius are analysed.

Five primary anemometers are located within The Heat Square at TGV, and are arranged at equivalent heights ($\approx 1.34m$). Each station is comprised of multiple instruments attached to a data logger. The two-dimensional locations are mapped in the most recent architectural drawing of THS layout. Locations are indicated as red dots with the station number attached in figure 3. The distance matrix computed between all points is presented in the appendix in table 9.

The square in this current layout has varied vegetation and paving surfaces installed in 2023, so vegetated surfaces are generally bare soil until summer. The photo attached shows the level of vegetation as of August 23rd 2023 4. The NE side of the square is planted with faster-growing vegetation compared to the SW side. By the end of this study, the vegetation at the NE side has changed by approximately 30 – 50cm underneath the anemometers on this side only—anemometers on the SW side record over effectively bare soil for the whole period.

4.d Additional Installation

Vertical profiling of wind shear is required to estimate aerodynamic parameters when using two-dimensional sonic anemometers. The established anemometer array is recording only at a single height, so an additional installation is necessary to enable the anemometric methodology outlined below in section 4.e.3. Two co-located anemometers are typically required to record for some time, so sufficient time stamps with neutral conditions are encountered. Additionally, multiple estimates per directional bin are required to estimate friction velocity and roughness length.

An ATMOS-22 anemometer was installed at a height of 207cm co-located with the Z6-20596 station. The location was decided to be desirable primarily because it was located furthest from any building. The height of the additional recording was a limitation set by materials available in the installation process. Ideally, a larger height difference would be possible for larger, more detectable shear and temperature measurement gradients.

Typically, a tower or other expensive wind profiling installations that collect estimates above the canopy height. Time and money is a limitation to this short research project so we attempt to gather some data from within the RSL, most probably the UCL and compare that to the GIS-based morphometric estimations. Parameter estimation using logarithmic wind law in the UCL is not typical and a clear contribution to uncertainty in this research.

The 'new' anemometer data is logged from August 25th and runs until September 9th. The measurement period is short and would ideally be installed longer for larger sample populations enabling better approximation of aerodynamic parameters. A photograph of the additional installation is attached as 5.



Figure 5: Two co-located anemometers are installed at station z6-20596 (August 25th, 2023)

4.e Methodology

4.e.1 Exploratory Data Analysis

The single-height sonic anemometer array within the square allows one to analyse the two-dimensional wind characteristics in The Heat Square. This phase is informative for future modelling approaches where aerodynamic parameters will be direction-dependent as wind approaches over various roughness elements. Heat flux estimations are sensitive to the aerodynamic parameters explored here, and an understanding of the frequency of direction and magnitude of speeds over time and space are informative for further research. This section attempts to address research question 1.

Data quality assessment is accomplished using a Python workflow for each station. The data is initially cleansed by assessing for zeros, null values and spurious outliers before assessment in the exploratory analysis. This first-pass analysis provides an overview of the local scale wind modification as compared to what is a relatively uninterrupted ambient wind flow from the EWI DAVIS station assumed to be in the ISL, not experiencing significant roughness-induced drag effects (see 2). We compare the 15-minute average wind speed and wind direction errors .

The 15-minute average wind speed and direction for the observation period are analysed and plotted using Python scripting for all stations. Direction is plotted using a wind rose diagram, which can be interpreted as a histogram plotted within a compass, whereby a wind sample coming from the north or within $\pm 5^\circ$ of 0° (or 360°) will be binned in that direction and is an intuitive visualisation of the frequency of wind directionality over a period.

Comparing wind speed spatial distribution across the square is accomplished using an error matrix showing mean error (ME) for all samples in the observation period. The mean error displays additive bias is chosen as a metric to display the relationship between stations that could be either over- or under-estimating relative to one another. If y is the target, and p is the prediction:

$$e = p - y \tag{4}$$

$$ME = \bar{e} \tag{5}$$

Where an overline (\bar{e}) indicates a mean of the total population. In the error matrix in 6 the predicted variable is on the vertical axis, which is intuitive since all stations are underestimating compared to the EWI station.

4.e.2 Stability Considerations

The ratio of buoyancy production to shear production is known as the Richardson number (Ri_f). When $Ri_f < 0$ conditions are unstable and turbulent kinetic energy TKE is produced by both shear and buoyancy. In stable conditions, on the other hand ($Ri_f > 0$) TKE is produced by shear and destroyed by buoyancy, when $Ri_f \approx 0$ no buoyancy is notable, only shear, known as *neutral conditions*. Close to the surface, the shear term is largest closest to the ground and as such wind shear is the more prominent contributor closer to the ground (Wyngaard and Coté, 1971; Moene and van Dam, 2014).

With regard to stability, it is imperative to filter all data for neutral conditions for which the logarithmic law applies. As discussed previously, the requirements are such that $Ri_f = 0$ for neutral conditions where only shear is the contributing factor to TKE. By calculating the Richardson number and filtering the data by that we obtain measurements for time stamps where the logarithmic profile is valid and will yield estimates of friction velocity and roughness length. The Richardson number is calculated as follows:

$$Ri_f = \frac{g\Delta\bar{\theta}_v\Delta z}{\bar{\theta}_v(\Delta\bar{u})^2} \tag{6}$$

Where g is the gravitational acceleration ($9.81ms^{-2}$), Δz is the height difference between the two wind speed sensors, $\Delta\bar{u}$ is the difference between the two temporally (15-minute) averaged

wind speeds. $\Delta\theta_v$ is the virtual potential temperature change. The virtual potential temperature in the denominator is averaged between the two measurement heights. Using the anemometer measurements we calculate Ri_f we can approximate L using the Richardson-bulk RI_b method where:

$$\frac{z}{L} = \begin{cases} \frac{10Ri_f}{1-5Ri_f} & \text{if } Ri_f \geq 0 \\ 10Ri_f & \text{if } Ri_f \leq 0 \end{cases} \quad (7)$$

As a form of stability control, we filter the wind measurements for timestamps that qualify as stable.

4.e.3 Anemometric Estimation

The logarithmic wind profile is generally accepted as valid within the Inertial Sublayer (ISL), which extends up to 200 meters above the Roughness Sublayer (RSL). However, this is mostly true under atmospherically neutral conditions, where the effects of buoyancy are negligible (i.e., $\frac{z}{L} = 0$ or $Ri_f = 0$). The extension of this profile's validity into the RSL is still a matter of ongoing research. Cheng and Castro (2002) posits that the vertical wind speed profile (U) can be reliably used within the RSL up to an average height H_{av} if a spatial average of the U profile is considered.

Thanks to newly installed equipment, we now have the capability to make observations at two different heights. This makes it possible to estimate the aerodynamic roughness length (z_0), a critical parameter for understanding wind behaviour near the surface. This estimation relies on the semi-empirical logarithmic wind law, as described by equation 1.

It's crucial to note that accurate estimation of both the zero-plane displacement height (z_d) and roughness length (z_0) typically requires atmospherically neutral conditions. This is because the logarithmic wind profile—and thus the formula for friction velocity—holds true under these conditions. Consequently, two co-located measurements are required for this purpose.

Anemometric methods require the two co-located measurements to determine the displacement and roughness parameters in the urban setting in neutral conditions. Usually, z_d and z_0 are assumed to be independent of stability but their estimation within this framework requires neutral conditions for the logarithmic wind profile to hold. Under neutral conditions, an expression for friction velocity from the log wind profile requires two co-located measurements:

$$u_* = \kappa \frac{\bar{u}(z_2) - \bar{u}(z_1)}{\ln\left(\frac{z_2}{z_1}\right)} \quad (8)$$

Using the friction velocity from 8 above, we can obtain estimates of roughness length with the following form:

$$z_0 = z_u \exp\left(-\frac{\kappa \bar{u}(z_u)}{u_*}\right) \quad (9)$$

Displacement height can be similarly determined by rearranging equation 1:

$$z_d = z_1 - \frac{z_2 - z_1}{\exp\left(k \frac{\bar{U}_{z_2} - \bar{U}_{z_1}}{u_*}\right) - 1} \quad (10)$$

Having determined u_* , z_0 and z_d for each neutral timestep we can compare the resulting values to the morphometric results.

4.f Morphometric Estimation

Morphometric methodologies directly incorporate the local morphology, by digital surface modelling and can account for varying micrometeorological cases (wind direction). Many morphometric methods exist, Kent et al. (2017) analysed and reviewed six methods in the context of central London and compared with anemometric methods and compared performances by extrapolating a wind profile using the parameter estimations. Results suggested that the most reliable estimates of aerodynamic parameters from two out of the six tested morphometric methods, the first from Millward-Hopkins et al. (2011) (MHO) and the second from Kanda et al. (2013) (KAN). These methods that include building height variability are seen to outperform anemometric methods when reproducing wind profiles to reference heights at 200m in high wind daytime scenarios. We investigate the aerodynamic parameters from those two methods here and two methods that use average building height (h_{av}), the 'rule of thumb' (RT) methodology and the method developed by Macdonald et al. (1998).

The RT methodology is based solely on the average roughness element height (H_{av}). The RT equations for z_0 and z_d are as follows:

$$RT_{z_d} = \alpha H_{av} \quad (11)$$

$$RT_{z_0} = \beta H_{av} \quad (12)$$

The coefficients 0.7 and 0.1 for α and β , respectively as determined by Grimmond and Oke (1999). We use the same symbology and subscript notation as in Kent et al. (2017) where the resulting parameters are subscripted to the method used.

The MAC method is developed to incorporate average height but distinguishes regular versus staggered arrays of roughness elements. The following equations summarise the approach used by the UMEP algorithm:

$$Mac_{z_d} = [1 + \alpha^{-\lambda_p} (\lambda_p - 1)] H_{av} \quad (13)$$

$$Mac_{z_0} = \left(\left(1 - \frac{z_d}{H_{uv}} \right) \exp \left[- \left\{ 0.5 \beta \frac{C_{Db}}{\kappa^2} \left(1 - \frac{z_d}{H_{av}} \right) \lambda_f \right\}^{-0.5} \right] \right) H_{av} \quad (14)$$

Here we see the introduction of λ_p , the plan area index, understood as the ratio of the building footprint to the area under consideration and λ_f the ratio of roughness element area facing wind. For displacement height (MAC_{z_d}) the constant α scales the increase of average height to displacement, determined by wind tunnel experiments. For roughness length Macdonald et al. (1998) introduces a building drag coefficient $C_{Db} = 1.2$ and the frontal area index. Values for α and β are adjusted for regular or staggered arrays.

The method after Millward-Hopkins et al. (2011) relates roughness element height standard deviation is as follows:

$$Mho_{z_d} = H_{av} \left[\frac{MhoU_{z_d}}{H_{av}} + \left((0.2375 \ln(\lambda_p) + 1.1738) \frac{\sigma_H}{H_{av}} \right) \right] \quad (15)$$

$$Mho_{z_0} = H_{av} \left[\frac{MhoU_{z_0}}{H_{at}} + (\exp(0.8867\lambda_f) - 1) \left(\frac{\sigma_H}{H_{av}} \right)^{\exp(2.3271\lambda_f)} \right] \quad (16)$$

Where:

$$MhoU_{z_0} = \left(\left(1 - \frac{z_d}{H_{av}} \right) \exp \left[- \left\{ 0.5 c_{Db} \kappa^{-2} \frac{A_f^*}{A_T} \right\}^{-0.5} \right] \right) H_{av} \quad (17)$$

$$\frac{MhoU_{z_d}}{H_{av}} = \left(\frac{19.2\lambda_p - 1 + \exp(-19.2\lambda_p)}{19.2\lambda_p [1 - \exp(-19.2\lambda_p)]} \right) \text{ (for } \lambda_p \geq 0.19) \quad (18)$$

$$\frac{MhoU_{z_d}}{H_{av}} = \left(\frac{117\lambda_p + (187.2\lambda_p^3 - 6.1) [1 - \exp(-19.2\lambda_p)]}{(1 + 114\lambda_p + 187\lambda_p^3) [1 - \exp(-19.2\lambda_p)]} \right) \text{ (for } \lambda_p < 0.19) \quad (19)$$

Where σ_H is the standard deviation of the roughness element heights, A^{*f} is the *unsheltered* frontal area of the building, A_T is the total area under consideration. By incorporating building height variability and surface-obstacle density the resulting z_0 and z_d parameters are intended to be representative of the wind profile above H_{av} i.e. valid within the RSL Millward-Hopkins et al. (2011).

The final morphometric method under consideration is from Kanda et al. (2013). Using horizontally-averaged turbulence statistics, Kanda et al. (2013) argued for an upper limit of z_d to be H_{max} rather than scaled by H_{av} :

$$Kan_{z_d} = [cX^2 + (a\lambda_p^b - c)X] H_{max} \quad (20)$$

Where a, b, c are 1.29, 0.36 and -0.17, respectively and X is the building height above the average, relative to H_{max} :

$$X = \frac{\sigma_H + H_{av}}{H_{max}}, \text{ for } 0 \leq X \leq 1 \quad (21)$$

$$Kan_{z_0} = (b_1 Y^2 + c_1 Y + a_1) Mac_{z_0} \quad (22)$$

Kan_{z_0} is an augmented formulation of Mac_{z_0} where a_1, b_1, c_1 are derived to be 0.71, 20.21 and -0.77, respectively. Y is implemented to allow for homogeneous arrays with $\sigma_H = 0$, defined as follows:

$$Y = \frac{\lambda_f \sigma_H}{H_{av}}, \text{ for } 0 \leq Y \quad (23)$$

Table 1: Morphometric Methods compared on the variables employed

Variable	H_{av}	λ_p	λ_f	H_{max}	σ_H
<i>Method</i>					
RT	✓				
MAC	✓	✓	✓		
MHO	✓	✓	✓		✓
KAN	✓	✓	✓	✓	✓

4.f.1 Implementation

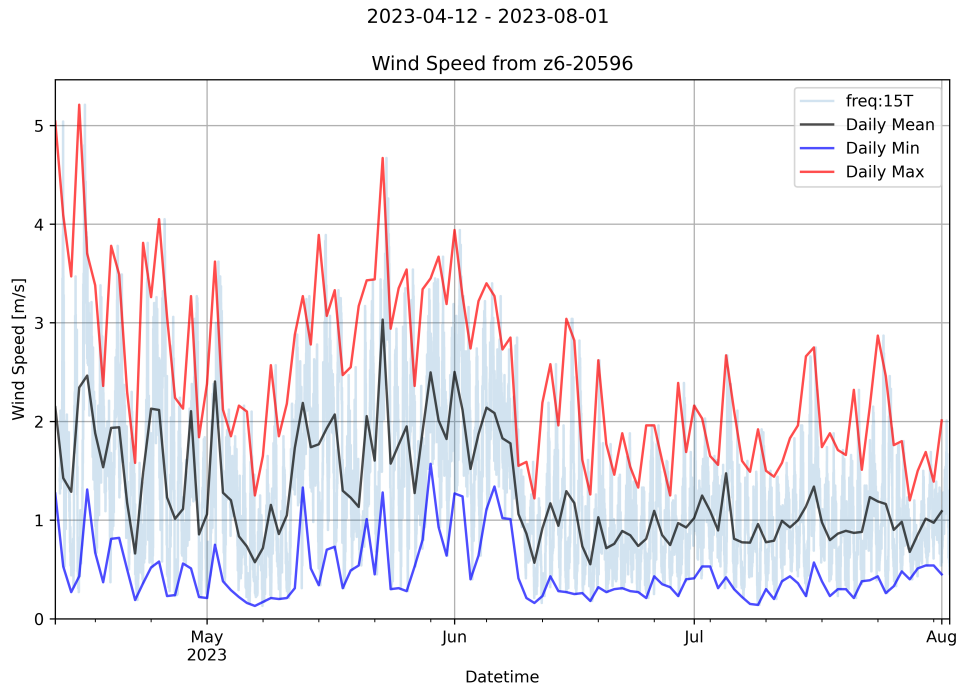
Using UMEP we compute these for all possible wind directions from every point of interest. The software requires a point, a search radius from within which the roughness elements are considered, and each directional search's width. For each of these four methodologies, we choose a search radius of 200m around each point of interest and calculate the resulting parameters for each 5-degree bin

around each point resulting in 72 directional estimates per parameter at each point. We implement two approaches to establish an understanding of the spatial and directional variability.

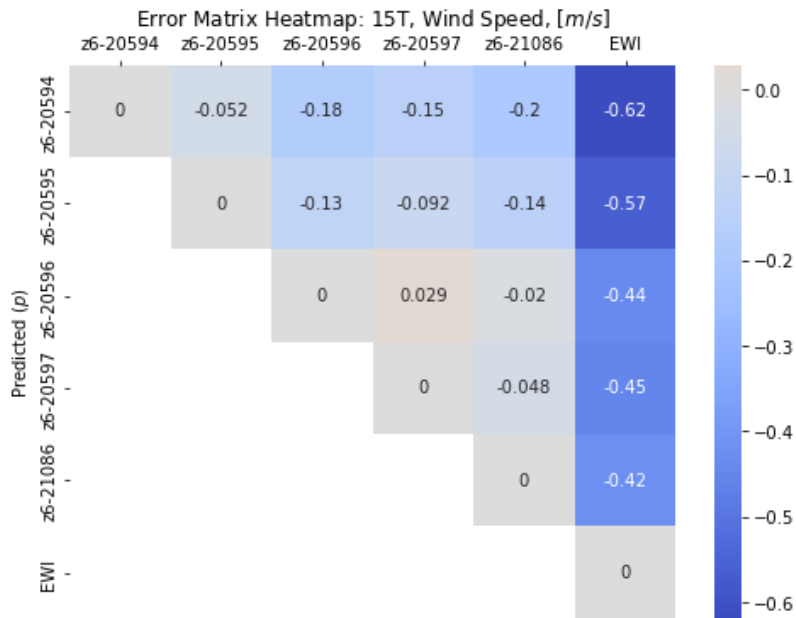
To analyse spatial variability we create an array of points in a 5m regularly spaced orthogonal grid within the bounds of THS. Additionally, we added a point at each anemometer location and three control points in the open water north of THS. The grid points are shown in figure 9 and those within the footprint of THS will be used to interpolate the isotropic results for each point to map and discuss the spatial variability and limitations of each methodology. The total number of points calculated sums to 53, calculated for 72 directional bins, for 4 different methodologies.

Spatial variability is assessed by mapping the isotropic results at each point and interpolating the results by Inverse Distance Weighting (IDW). IDW is a geostatistical interpolation method that estimates unknown values at unmeasured locations based on known data points within a given area. The technique calculates the weighted average of nearby known points to predict the value at an unknown location, with the weight inversely proportional to the distance from the known points to the target point. In other words, closer points are given more weight in influencing the estimation, while points farther away contribute less. The IDW distance coefficient, often denoted as p , controls the influence of known points on the interpolated values; a higher value of p gives more weight to points closer to the target location, resulting in a less smooth surface, while a lower value produces a smoother interpolation but may underemphasise the impact of nearby points. Performing IDW in QGIS with a 5-meter grid we choose an IDW distance coefficient of 4 as an optimal choice for the scale and density of measurement.

5 Results and Discussion



(a) Station Z6-20596



(b) Station Z6-20594

Figure 6: (a) Time series displaying the wind speeds recorded at station z6-20596 through the period of installation (b) Error matrix computed with mean average error between all stations in ms^{-1}

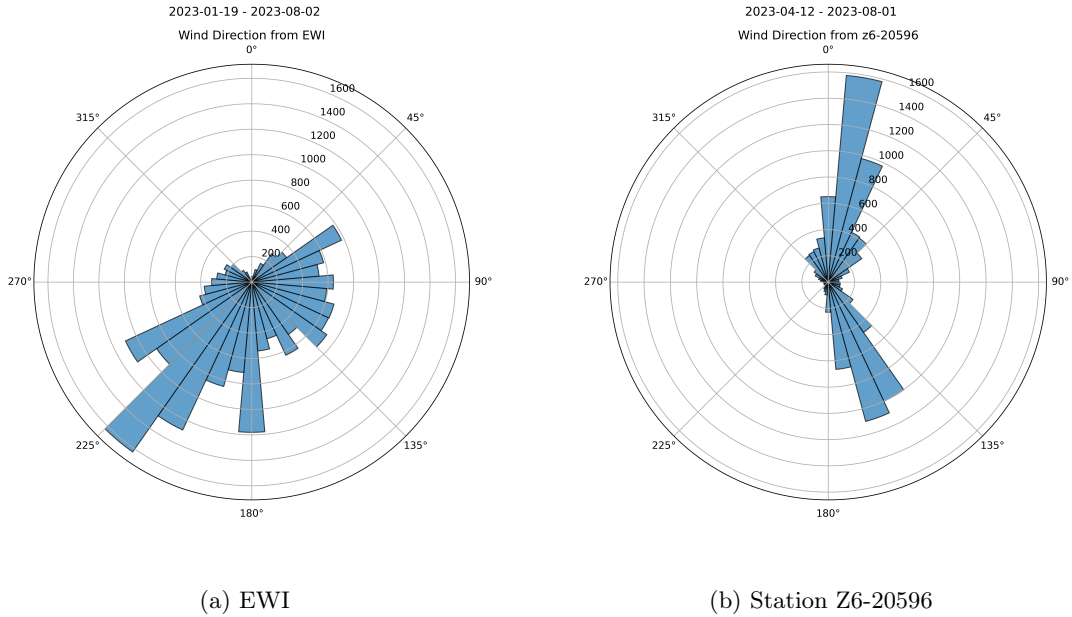


Figure 7: Two wind rose charts relating to 15 minute resampled data for (a) the EWI DAVIS weather station at 100m and (b) the most northerly station Z6-20596.

5.a Exploratory Analysis

5.a.1 Wind Speed

Understanding the variability of wind speed indicates the spatial and seasonal variability of wind across the square (refer to Figure 3 for locations). This analysis can assist in identifying the spatial considerations necessary for making accurate aerodynamic estimates from a single location or for the square as a whole. To examine the seasonal variability of wind speed, we analyse a time series for the northernmost anemometer in the square (z6-20596, Figure 6a). For the spatial variability within the square, we present an error matrix featuring the Mean Error (ME) (Figure 6b). Both figures are generated from mean horizontal wind speeds, recorded and averaged at a 15-minute frequency, spanning from April to August 2023. The time series features daily maxima and minima, represented by red and blue enveloping lines.

The time series for station z6-25696 (image a) reveals a highly variable wind speed from April to mid-early June, punctuated by a minimum in early May where the daily maxima and minima are most closely situated. A period of reduced variability is observed after mid-June, characterised by lower average daily wind speeds. Specifically, from mid-June to late July, the daily maxima are approximately 30% lower and the daily mean winds are roughly 50% lower compared to earlier months. When comparing the northern station (z6-25696) to the southern station (z6-20594, see Appendix Figure 14), the northerly station shows higher mean wind speeds (≈ 1 m/s) and maxima (≈ 1.9 m/s) than the southern station (≈ 0.75 m/s and ≈ 1.75 m/s, respectively) after mid-June.

Spatial variability of wind speeds among stations within the square is best captured by an error matrix. This matrix reveals that the most southerly station, z6-20594, consistently records lower

wind speeds than other THS stations. The most significant negative error (-0.2) is observed between this station and z6-21086, which is located 13 m to the northwest and happens to be the closest station. On the other hand, z6-20186 registers higher average wind speeds than all other stations. The absolute errors across the heat square for the entire period are ≤ 0.2 m/s. A noticeable gradient of decreasing average wind speed from north to south is evident along the northeast side of the square. This gradient is more pronounced than the one observed with only two points (z6-21086 and z6-20594) along the southwest side. The variations between stations on the southwest side suggest the presence of a more complex wind pattern, potentially influenced by proximity to the co-creation centre.

The EWI station is located to the northwest of the heat square and is elevated 100 m above the ground (≈ 99 m a.s.l). It is situated at a distance of ≤ 369 m from the THS stations. On average, wind speeds at this location are $+0.5$ m/s faster compared to the reference ground level.

5.a.2 Wind Direction

The wind roses presented in Figure 7 reveal ontrasting wind direction distributions between two stations. Subfigure (a) showcases the wind direction distribution from the EWI station, which is presumed to be situated above the influence of urban roughness in the Inertial Sublayer (ISL). Since March 2023, this station has recorded a skewed wind distribution, with the prevailing wind direction most frequently originating between $215^\circ - 225^\circ$. This is a typical pattern for this Northern European locality influenced by warm Atlantic ocean currents. Interestingly, the EWI station has recorded almost no winds coming from a northerly direction.

In contrast, the local wind direction sample from the north of The Heat Square (THS) demonstrates distinct characteristics within the Urban Canopy Layer (UCL). This sample displays a bimodal wind distribution. The primary peak, comprising over 1600 samples, occurs between $5^\circ - 15^\circ$, while the secondary peak, with over 1000 samples, lies between $155^\circ - 165^\circ$. The primary peak corresponds to an open area to the NNE of the station, while the secondary peak aligns with the NNW-SSE orientation of the main axis of THS, which has a bearing of $340 - 160^\circ$.

Further observations from other stations within THS can be seen in Figure 8. Most of these stations show a primary wind direction that is generally aligned with the long axis of THS, originating mostly from 340° . This is in contrast to the z6 - 20596 station located at the north of THS, which shows less influence from the urban 'canyon' effect, and therefore is less aligned with the surrounding buildings. This suggests that the canyon effect, which typically aligns wind flows with the building walls, is dominant for most stations deeper within THS.

5.a.3 Roughness Elements in the Digital Surface

The Digital Elevation Model (DEM) and Digital Surface Model (DSM) used in this study cover a total search area of $211,001m^2$. Summary statistics of these models are provided in Table 2. The primary difference between the DSM and DEM is that the DSM includes roughness elements, whereas the DEM offers only a baseline representation of the land surface.

Within the search area, the tallest roughness element has an elevation of $42.59m$, which corresponds to the TU Delft Science Center building located approximately $126m$ east of The Green

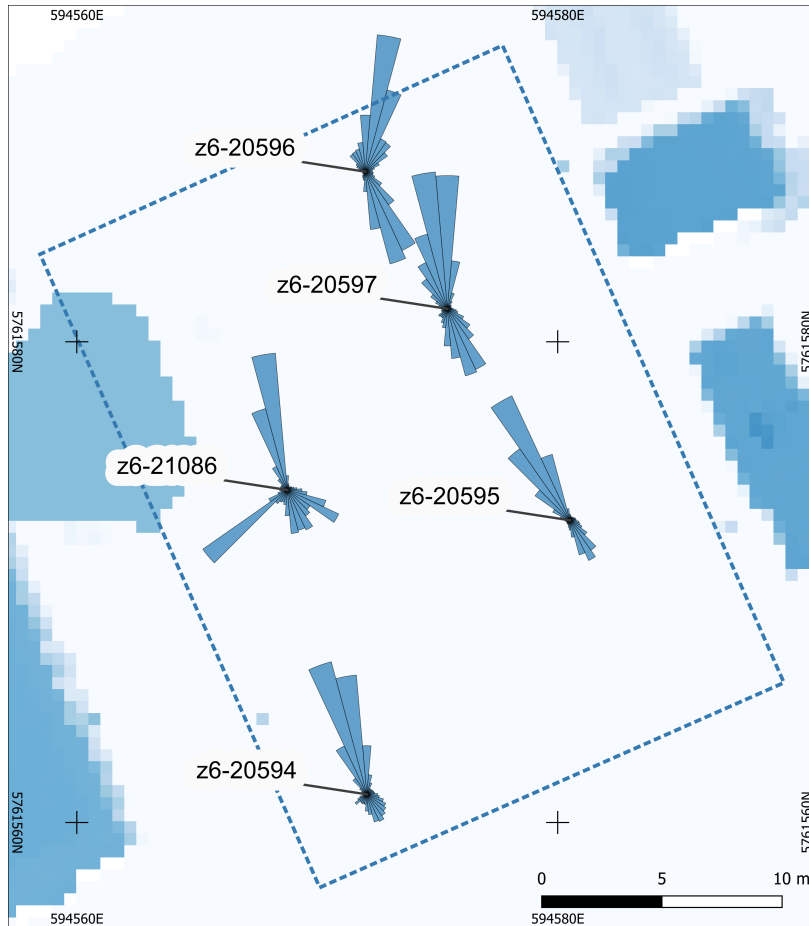


Figure 8: The Heat Square map overlain with wind roses displaying the frequency of the wind directions at each anemometer.

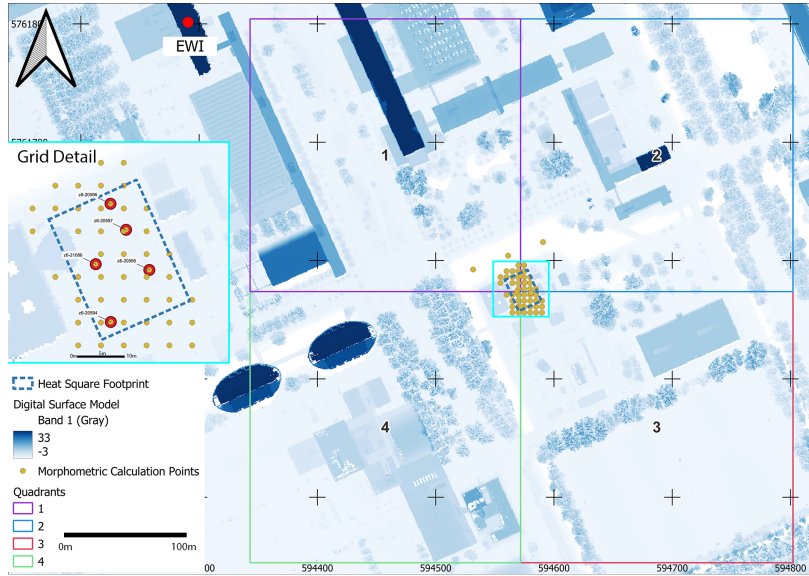


Figure 9: Four quadrants for zonal statistics displaying the distribution of roughness element characteristics in the space.

Village (TGV). The second tallest structure is the Civil Engineering building, with a height of $\leq 39m$ and located $129m$ NNW of The Heat Square (THS). For a more detailed breakdown, summary statistics and search grid points are illustrated in Figure 9.

Quadrant 1, spanning from 270° to 360° as shown in Figure 9, features open green spaces and two tall buildings aligned along a $340^\circ - 160^\circ$ axis. Quadrant 2 has similar characteristics but includes denser vegetation at the edge of the search radius and the tallest building. Quadrant 3 is an open playing field with scattered mature trees and one significant building. Quadrant 4, from 180° to 270° , is the most diverse in terms of roughness elements, comprising two large residential buildings, a sports complex, and a mature tree grove.

According to the review by Grimmond and Oke (1999), all quadrants fall at the lower limit (Quadrant 1) or even below the mean height (Quadrants 2-4) to be considered a low-height and low-density urban setting.

Table 2: Within the footprint of all combined surface areas the summary statistics of both the digital surface and digital elevation models are presented, additionally the summary statistics of the quadrants in 9 are attached

Whole Area	Quadrant	Mean	Median	stDev	Min	Max
<i>DSM</i>		3.3	-0.69	7.41	-3.78	42.59
<i>DEM</i>		-1.11	-1.09	0.53	-3.86	2.9
	1	5.36	-0.09	9.1	-3.11	39
	2	2.29	-0.87	5.82	-3.78	42.59
	3	0.92	-1.11	4.25	-3.19	31.08
	4	3.67	-0.5	7.54	-3.14	37.16

5.b Aerodynamic Parameter Estimation

5.c Data Issues

Installing the anemometers for this short-term research project encountered several limitations that have had implications for the study. The most notable issue was the low installation height of the anemometers, which compromised the calculations for the virtual potential temperature gradient $\Delta\theta_v$. It is not optimal to install anemometers so low, specifically within the UCL. Secondly, too closely spaced anemometers do not capture a sufficient range of temperature gradients. As a result, the calculated gradient often becomes zero. This affects the Richardson number equation, leading to overrepresenting timestamps categorised as neutral conditions after filtering. This introduces significant uncertainty in the estimation of roughness parameters.

Furthermore, we encountered data availability issues with the EWI station intended to serve as a reference for estimating logarithmic wind profiles. The initial plan was to utilise data from the EWI station for extrapolating wind profiles, thereby assessing the performance of various parameter sets. However, during the analysis phase, it became evident that the EWI station's data recording protocol changed in August, switching from comma-separated value (CSV) files to netCDF (NC) format. As of writing the NC files on the server are blank for wind speed. Unfortunately, this change coincided with the operational period of our co-located anemometer setup. As a result, reference wind speed data from the EWI station is unavailable for direct comparison during the relevant time frame. This further complicates our ability to assess the reliability of our parameter estimations.

5.d Spatial Variability Within The Heat Square

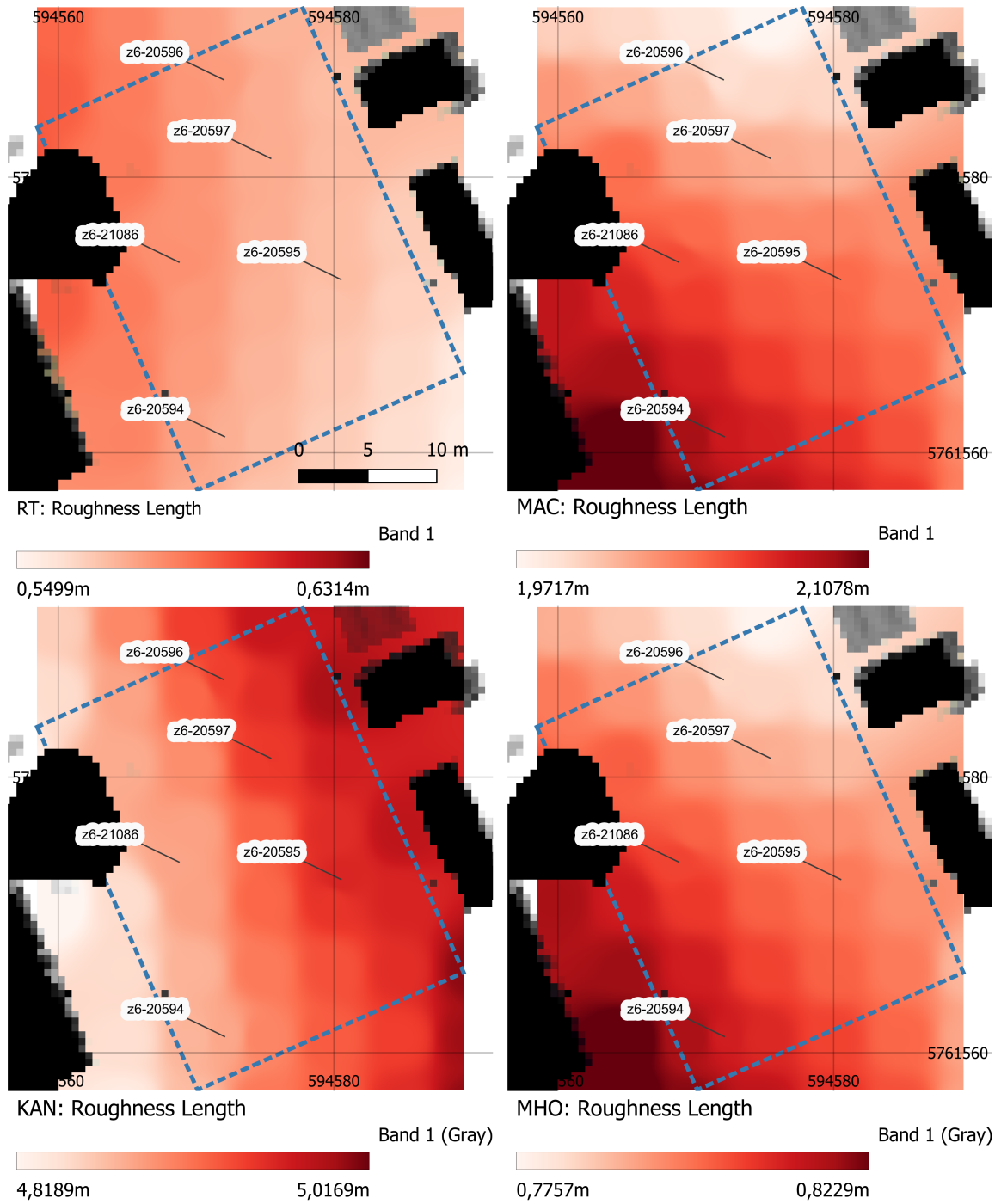


Figure 10: Comparison of interpolated isotropic roughness length estimates in the heat square.

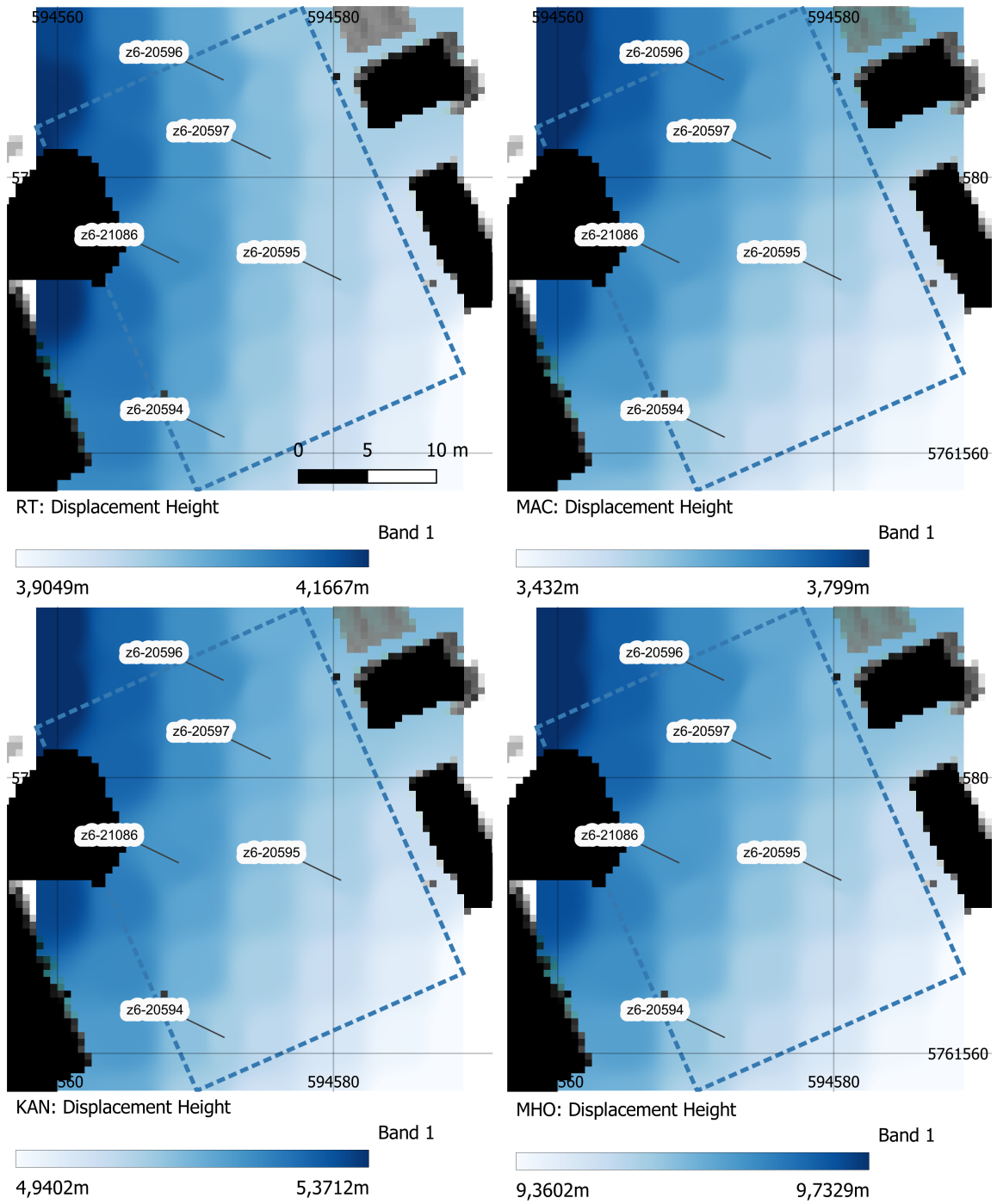


Figure 11: Comparison of interpolated isotropic roughness length estimates in the heat square.

Figures 10 and 11 display interpolated isotropic roughness length estimates across The Heat Square, revealing significant inter-method spatial variability. Inverse Distance Weighting (IDW) estimates for z_0 are remarkably divergent, presenting conflicting gradients across the area. All four employed morphometric methods—depicted in color gradients from white ($\bar{z}_0 - 2\sigma_{z_0}$) to dark red ($\bar{z}_0 + 2\sigma_{z_0}$)—vary significantly in their range and mean. Comprehensive comparisons of isotropic roughness estimates for all grid points, monitoring stations, and open-water points are tabulated in Tables 3 and 4 for z_0 and z_d , respectively.

The RT_{z_0} method indicates a low and narrow range of values, exhibiting a positive gradient from the southeast to the northwest. These estimates align with a "Low height and density" urban setting, according to the typical values cited in Grimmond and Oke (1999). Conversely, MHO_{z_0} reveals an almost inverse gradient but also falls within the "Low height and density" category. MAC_{z_0} and KAN_{z_0} present significantly higher estimates, with MAC_{z_0} being approximately 2.6 times higher than MHO_{z_0} . These larger values would classify the environment as "High-rise... with multistory tower blocks" based on the same source.

For displacement height (z_d), all methods exhibit a similar gradient pattern but differ in their value ranges. Lower estimates are generally located in the southeast, while higher ones appear in the northwest. According to Grimmond and Oke (1999), typical displacement heights for urban settings are classified into three categories: low, medium, and high height and density, with respective ranges of $2 - 4m$, $3.5 - 8m$, and $7 - 15m$.

5.e Anisotropic Parameter Variability

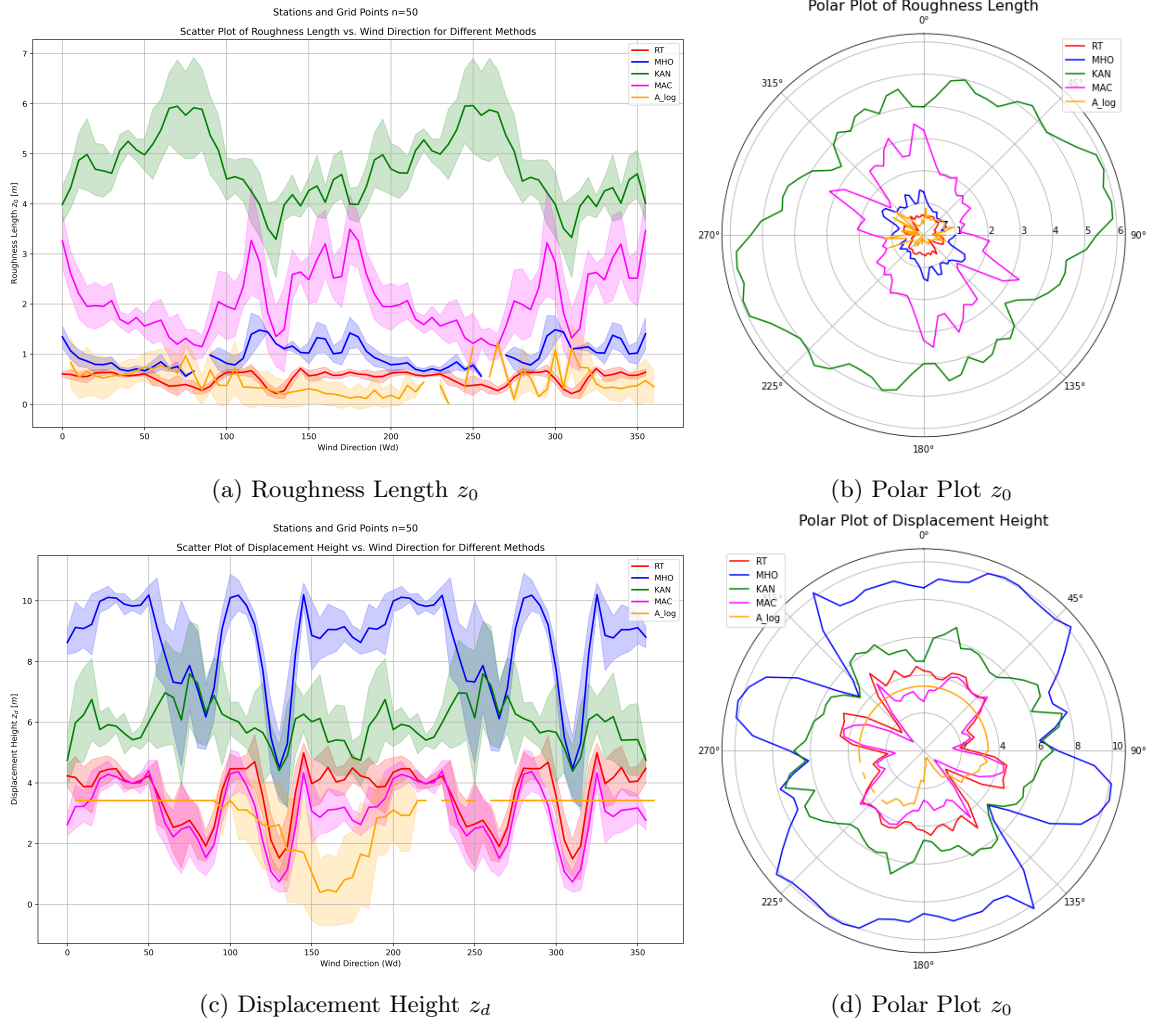


Figure 12: Four plots showing the range of aerodynamic parameter estimations z_0 (a, b) and z_d (c, d). Four morphometric methodologies are presented for comparison with anemometric roughness additionally included in (a) and (b). Shading in the line plots represents $\pm 1\sigma$ (standard deviation).

Figure 12 presents two sets of anisotropic estimates for roughness length z_0 and displacement height z_d . Each estimate encompasses a 200m radius and is divided into 5° directional bins, covering a total area per bin of $1745m^2$. Values are linked to monitoring stations, a 5m grid, and 'open-water' sample points. Line plots help elucidate uncertainties associated with each 5° bin, providing insights into spatial variability across the square. Polar plots facilitate a more intuitive understanding of the data in relation to the square's physical geography.

For the prevailing wind direction of 340° , anemometric results A_{log,z_0} display a mean roughness

length of $0.3535m \pm 0.18$. According to Kent et al. (2017), a minimum of 20 measurements per directional bin is needed for reliability, making our result credible although its standard error is high ($\approx 50\%$). The anemometric method reveals its highest variability between $210^\circ - 310^\circ$, generally coinciding with tall mature trees in quadrant 3 (see Figure 9). These results align closely with the Grimmond and Oke (1999) review, which indicates that such values correspond to low height and density urban areas.

The KAN_{z_0} method is highest with an isotropic mean value of $4.9m \pm 0.034$. With regard to the 340° bin, the prevailing wind direction, the value is lower than the isotropic mean at 4.02 ± 0.32 , all prevailing wind directional results are attached in the appendix as 11. RT_{z_0} presents the lowest estimates across above A_{log,z_0} the square ($0.576m \pm 0.004$) just below MHO ($0.798m \pm 0.01$). MAC_{z_0} represents the middle ground estimate with some significant directional sensitivity. KAN_{z_0} method produces an inverse direction dependence to the other methods whereby estimates in the E-W ($90 - 270^\circ$) are maximum for this method whereas these are minima for other methods. The MAC_{z_0} , KAN_{z_0} and MHO_{z_0} methods are lower and show decreasing directional-dependent sensitivity. MHO_{z_0} shows a highly discontinuous series with values that seem to agree with the RT_{z_0} estimates generally. These minima are coincident with the wind directions that have lower average roughness element height H_{av} , lower variability of elements σ_H , and low max element height H_{max} (see appendix figure 16 and the resulting 17 for H_{av} and λ_f , respectively).

Regarding anisotropic displacement height, z_d estimation comparison in (a,b) of figure 12. Here the MHO_{z_d} estimates are, by contrast to their previous rank, higher than the KAN_{z_d} estimates (9.55 ± 0.01 vs 5.158 ± 0.057 , respectively). MAC_{z_d} estimates are the lowest and are almost equivalent to the KAN_{z_d} values (3.619 ± 0.054 vs 4.035 ± 0.028 , respectively). Similar minima are observed as is noted in roughness length results above, corresponding with minimal roughness element height variability and low maximum roughness element height. The anemometric calculation method A_{log,z_d} results in a constant value of $3.42m$ that is unchanging with wind speed or direction except for within a directional window from $100^\circ - 210^\circ$. The mean in this region shows a semi-symmetric minima across this window, and corresponds with winds approaching over THS.

Table 3: All morphometric isotropic estimates for displacement height, z_0 , are presented as a mathematical mean and a standard deviation.

	MHO		KAN		MAC		RT	
	<i>mean</i> [m]	<i>stDev</i>	<i>mean</i>	<i>stDev</i>	<i>mean</i>	<i>stDev</i>	<i>mean</i>	<i>stDev</i>
Grid (n=45)	0.799	0.013	4.917	0.057	2.040	0.039	0.576	0.012
Stations (n=5)	0.798	0.010	4.926	0.034	2.035	0.031	0.576	0.004
Water (n=3)	0.766	0.032	4.918	0.225	1.924	0.072	0.588	0.033

Table 4: All morphometric isotropic estimates for displacement height, z_d , are presented as a mathematical mean and a standard deviation.

	MHO		KAN		MAC		RT	
	<i>mean</i> [m]	<i>stDev</i>	<i>mean</i>	<i>stDev</i>	<i>mean</i>	<i>stDev</i>	<i>mean</i>	<i>stDev</i>
Grid (n=45)	9.539	0.122	5.148	0.140	3.608	0.121	4.031	0.083
Stations (n=5)	9.550	0.052	5.158	0.057	3.619	0.054	4.035	0.028
Water (n=3)	9.742	0.260	5.382	0.336	3.842	0.257	4.119	0.234

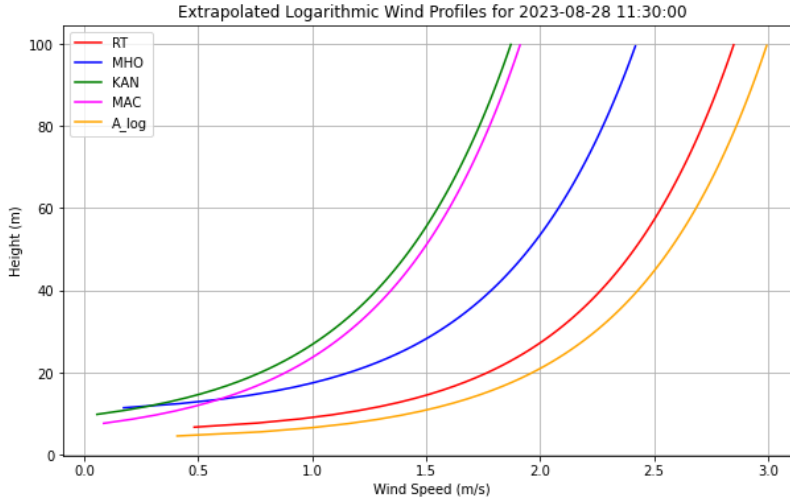


Figure 13: Five methods are compared by extrapolating on a typical day at prevailing 340° wind conditions.

5.f Profile Extrapolation Comparison

Table 5: Comparison of Wind Speed Estimations Using Different Methods with parameters derived for an instance of wind direction from 340°

Method	z_0	z_d	u_*	Wind Speed at z_{2m}	Wind Speed at z_{100m}
RT	0.7242	5.0692	0.2340	0.8446	2.8518
MHO	1.4383	9.5028	0.2340	0.9661	2.4224
KAN	3.8349	5.6107	0.2340	-0.0352	1.8735
MAC	3.6571	3.4196	0.2340	-0.5535	1.9147
A_log	0.5742	3.4200	0.2340	0.5296	2.9976

In applying the logarithmic wind law to extrapolate wind profiles, parameters derived from a neutral instance with a wind direction of 340° were utilized. Interestingly, the *RT* and A_{\log} methodologies align closely with the anemometrically-derived parameters, yielding the highest mean profile velocities. On the other hand, the methods based on standard deviation of height σ_H (*MHO* and *KAN*) yield wind speeds at $100m$ that are approximately 30% lower than those extrapolated by *RT* and A_{\log} .

The resemblance between the *MHO* and *KAN* methods is noteworthy, despite their contrasting aerodynamic parameters. This observation underscores the compensatory nature of parameters in the logarithmic wind law: variations in one can be balanced by the other. Specifically, *MHO* serves as a mid-range estimate, extrapolating to a wind speed $U(z_{100m}) = 2.42 \text{ m/s}$.

Including the calculated wind speed at $2m$, $U(z_2)$, sheds light on the challenges of wind profile extrapolation below the roughness sublayer (RSL). At this specific time, the observed wind speed was $U(z_2) = 0.75 \text{ m/s}$, which most closely aligns with the predictions from the *RT* and anemometric

methods.

6 Discussion

6.a Modification and Morphology

Prevailing conditions in our study strongly suggest that the wind modification occurring within the Roughness Sublayer (RSL) plays a pivotal role in shaping the micrometeorological characteristics of THS. The initial exploratory analysis served to prioritise and inform the subsequent parameter estimation phase. Notably, vertical errors in wind speed were found to be more significant than horizontal errors. Any wind speed data from the EWI station, which is spatially dislocated by approximately $360m$ from the ground stations, should be interpreted cautiously.

Horizontal wind speed errors between THS stations provide valuable insights into how building morphology impacts wind flow patterns. Our observations indicate that wind speeds along the north-east side of the square are attenuated in a north-to-south direction. This area is characterised by its parallel alignment with local building morphology and overlying vegetation. Conversely, stations on the southwest side (specifically z6-21086 and z6-20594) display a larger speed gradient, seemingly unaffected by seasonal vegetation growth. Therefore, building morphology rather than vegetation appears to be the dominant roughness element affecting wind flow at this scale.

Wind direction data further corroborates the governing role of building morphology. Contrary to mesoscale wind directions, which are primarily southerly, winds traversing the square are predominantly northerly. As illustrated in Figures 6 and 8, these microscale wind patterns are effectively antithetical to those observed at the EWI station, supporting the hypothesis that building morphology is the primary driver for these deviations. The influence of roughness elements manifests in the directional turning of winds, particularly from North to South, through the square.

Analysis of Figure 8 reveals a directional shift from northwest to northeast (approximately 340°), suggesting channeling effects caused by the buildings. Exceptions to this pattern occur at less-sheltered stations like z6-20596 and z6-21086. The least bimodal distribution was observed at z6-20594, which is situated farthest from the main flow direction intersecting the square.

To summarize, the dominant wind direction within THS aligns approximately with the long axis running from northwest to southeast ($340^\circ \pm 5^\circ$). Although the exact impact of external roughness elements is not quantitatively known, the stark divergence between local and EWI station data implicates external building and vegetation structures as primary determinants of wind behavior at a meter scale. These observations serve to guide the selection of appropriate aerodynamic parameters for future modeling efforts.

6.b Parameter Estimations

6.c Aerodynamic Roughness Length

Five distinct methodologies were applied to estimate z_0 , each yielding varied outcomes and interpretation nuances. Among these, A_{log,z_0} and MHO_{z_0} showed a commendable agreement with the

widely recognized RT_{z_0} methodology. Interestingly, the discrepancy between anemometric and morphometric methods in this study is substantially smaller than that found in Kent et al. (2017), where eddy covariance techniques are used to estimate z_0 and z_d . Negative discrepancies in some of the z_0 estimates were more frequent in areas characterised by low average roughness element height and low variability. These observations resonate with prior studies suggesting that densely packed roughness elements, such as trees, induce a flow pattern that is more akin to skimming than chaotic turbulence Kent et al. (2017); Oke and Cleugh (1987).

Contrastingly, the KAN_{z_0} method deviated significantly from expected values and even displayed opposing directional sensitivities. This is particularly intriguing when juxtaposed with the results presented in Kent et al. (2017), where KAN_{z_0} seemed to be well-aligned with MAC_{z_0} within a 1-2m range. Our study environment’s higher density could partially explain this discrepancy. However, a more plausible cause appears to be the added sensitivity of the plan area index, λ_p , as shown in Figure 18 and evident from Equation 22.

Interestingly, MHO_{z_0} values consistently fall below those of MAC_{z_0} , contrasting findings from comparative studies. While MAC_{z_0} values align reasonably well with experimental results, MHO_{z_0} falls noticeably below the expected range. This lower estimation range for MHO_{z_0} may be attributed to elevated values of λ_f . According to Equation 16 and as illustrated in Figure 17, maximum MHO_{z_0} values are likely to occur at lower λ_f values, contrasting with MAC_{z_0} , which peaks in areas of high λ_f .

6.d Zero-Plane Displacement

In the comparison of four morphometric methodologies for estimating z_d , the MHO_{z_d} approach yields conspicuously higher values, standing in stark contrast to the RT_{z_d} method. Echoing findings from the study by Kent et al. (2017), methodologies that incorporate variability, denoted by σ_H , consistently produce higher z_d estimates compared to those based solely on the average height H_{av} . This dichotomy between the two sets of methodologies is illustrated by their different consistency with established theoretical bounds: KAN_{z_d} and MAC_{z_d} are in line with $z_d \geq 1.5H_{av}$, whereas H_{av} -based methods more closely align with $z_d \geq 0.7H_{av}$. The latter is in agreement with the roughness sublayer (RSL) depth estimate proposed by Roth (2000), while the former resonates with later suggestions by Barlow (2014).

The A_{log,z_d} estimate is particularly noteworthy; it largely concurs with the $0.7H_{av}$ approximation when considering the first quadrant to the northwest, where $H_{av} = 5.36m$. However, the method’s tendency to yield a single, invariant value for all wind directions—except for the variable window to the south—suggests that its formulation may not be fully optimized for this application. This highlights the need for either an improved formulaic approach or a more robust experimental design to better capture directional variability in z_d .

7 Conclusions and Recommendations

The efficacy of various methodologies for estimating wind profiles is contingent on the unique characteristics of the study site, including building orientation and morphology. Although methods like KAN_{z_0} and MHO_{z_0} , which incorporate height variability, were previously found to be most accurate across different settings Kent et al. (2017), their applicability to The Heat Square remains questionable. The parameters derived using these methods fall outside of the generally accepted ranges in literature Grimmond and Oke (1999); Kent et al. (2017).

Our anemometric estimates most closely align with the RT morphometric methodology, particularly when it comes to profile extrapolation. Nevertheless, the absence of inertial sub-layer (ISL) wind speed data hampers our ability to decisively identify the most suitable parameter set for heat flux estimations. Based on the data currently available, the RT method emerges as the most robust for our specific study area.

The scope of this research could be significantly expanded by exploring how different zero-plane displacement parameters affect heat flux calculations. However, this analysis is currently constrained by two significant limitations. First, time constraints did not allow for such an in-depth study to be conducted. Second, the inadequate separation between the co-located sensors has led to difficulties in estimating the virtual potential temperature.

The current analysis remains incomplete due to a data gap for this study period's ISL wind speed measurements. Future research should prioritise filling this gap by communicating with the administrators of that data source and expanding upon the preliminary work done here. Additional time and resources should be allocated to generate reliable field estimates, particularly in The Heat Square and The Green Village. We strongly recommend that future efforts focus on improving anemometric estimates' robustness.

A Code and Data Repositories

<https://github.com/manrahan/TGVaero.git>

The code repository is cloned using the link above.

<https://drive.google.com/drive/folders/16gTWOFe2ItO5gsLR7aAUnpdFfYY9MIE5?usp=sharing>

The data folder can be downloaded and situated in the same folder as the code folder. The data accessed via the link above, access is set to restricted.

<https://drive.google.com/drive/folders/1N7zGYRUCnGvwi-K2RpVb2x28NZB4lgo?usp=sharing>

UMEP outputs are attached above in the folder above (open access).

<https://drive.google.com/drive/folders/15CmVyelZ4HTOsQ6AESlCVLRYjIvVf9mP?usp=sharing>

The above link is for the GIS data and GIS project used to create layouts and plots.

B Additional Equations

The following are the underpinning flux-gradient equations relating to momentum and heat using MOST, adapted from Moene and van Dam (2014):

$$\int_{z_{u1}}^{z_{u2}} \frac{\partial \bar{u}}{\partial z} \frac{\kappa z}{u_*} dz = \int_{z_{u1}}^{z_{u2}} \phi_m \left(\frac{z}{L} \right) dz \iff \bar{u}(z_{u2}) - \bar{u}(z_{u1}) = \frac{u_*}{\kappa} \left[\ln \left(\frac{z_{u2}}{z_{u1}} \right) - \Psi_m \left(\frac{z_{u2}}{L} \right) + \Psi_m \left(\frac{z_{u1}}{L} \right) \right] \quad (24)$$

$$\int_{z_{\theta1}}^{z_{\theta2}} \frac{\partial \bar{\theta}}{\partial z} \frac{\kappa z}{\theta_*} dz = \int_{z_{\theta1}}^{z_{\theta2}} \phi_h \left(\frac{z}{L} \right) dz \iff \bar{\theta}(z_{\theta2}) - \bar{\theta}(z_{\theta1}) = \frac{\theta_*}{\kappa} \left[\ln \left(\frac{z_{\theta2}}{z_{\theta1}} \right) - \Psi_h \left(\frac{z_{\theta2}}{L} \right) + \Psi_h \left(\frac{z_{\theta1}}{L} \right) \right] \quad (25)$$

Equations that describe the vertical differences in scalars relating to momentum in equation 24 and heat in equation 25. κ is the Von Carman constant, 0.40. $\frac{z}{L}$ is a stability parameter equivalent to the Richardson number and L is the Obhukov length. Ψ_m and Ψ_h are the integrated flux-gradient relationships. For derivations of the Ψ functions and relations to atmospheric resistance read Moene and van Dam (2014) and Wilson (2001).

C Additional Tables

Table 6: Data loggers/Stations in The Heat Square with the count of the variables logged at each station. Abbreviations: SWC (Soil Water Content), STemp (Soil Temperature), SSCond (Soil Saturation Conductivity), MP (Matric Potential), RAP (Reference Air Pressure), WS (Wind Speed), WD (Wind Direction), AT (Air Temperature), GS (Gust Speed).

Station	SWC	STemp	SSCond	MP	RAP	WS	WD	AT	GS
Z6-20594	4	5	3	1	1	1	1	1	1
Z6-20595	4	5	3	1	1	1	1	1	1
Z6-20596	3	4	2	1	1	2	2	2	2
Z6-20597	4	5	3	1	1	1	1	1	1
Z6-20600	2	2	1	-	1	-	-	-	-
Z6-21086	4	5	3	1	1	1	1	1	1

Table 7: Variables recorded at each station, the respective unit and instrument.

Variable	Unit	Logger	TEROS 11	TEROS 12	TEROS 32	ATMOS 22
Reference Pressure	<i>kPa</i>	x			x	
Temperature	<i>celcius</i>	x				
Saturation Conductivity	<i>ms/cm</i>			x		
Water Content	<i>m3/m3</i>		x	x		
Soil Temperature	<i>celcius</i>		x	x	x	
Matric Potential	<i>kPa</i>				x	
Absolute Pressure	<i>kPa</i>				x	
Wind Direction	<i>degrees</i>					x
Wind Speed	<i>m/s</i>					x
Gust Speed	<i>m/s</i>					x
Air Temperature	<i>celcius</i>					x

??

Table 8: ATMOS 22 horizontal anemometers per station with respective heights, date ranges of availability and frequency of recording.

Station Name	Height [cm]	Anemometer 1		Date To	Height	Anemometer 2		Frequency
		Date From	Date To			Date From	Date To	
Z6-20594	<i>136</i>	12/04/2023	Present					15min
Z6-20595	<i>135</i>	12/04/2023	Present					15min
Z6-20596	<i>135</i>	12/04/2023	Present		<i>207</i>	26/08/2023	Present	15min
Z6-20597	<i>134</i>	12/04/2023	Present					15min
Z6-21086	<i>133</i>	12/04/2023	Present					15min

Table 9: The distance matrix for all anemometers used in the analysis

Distance	z6-21086	z6-20594	z6-20595	z6-20596	z6-20597	EWI
z6-21086	-	13.09m	11.82m	13.64m	10.06m	358.53m
z6-20594	13.09m	-	14.19m	25.91m	20.48m	369.18m
z6-20595	11.82m	14.19m	-	16.82m	10.17m	368.49m
z6-20596	13.64m	25.91m	16.82m	-	6.65m	352.88m
z6-20597	10.06m	20.48m	10.17m	6.65m	-	359.06m
EWI	358.53m	369.18m	368.49m	352.88m	359.06m	-

Table 10: Values for all variables at the prevailing wind direction at all points in the grid calculation showing mean (overline) and standard deviation (σ)

At 340°	$\overline{H_{av}}$ [m]	$\sigma_{H_{av}}$ [m]	$\overline{\lambda_p}$	σ_{λ_p}	$\overline{\lambda_f}$	σ_{λ_f}	$\overline{H_{max}}$ [m]	$\sigma_{H_{max}}$ [m]	σ_H [m]	σ_{σ_H} [m]
All Methods	6.4360	1.0049	2.50E-04	5.39E-05	0.28125	0.07854	10.01600	0.00374	4.67648	0.2763

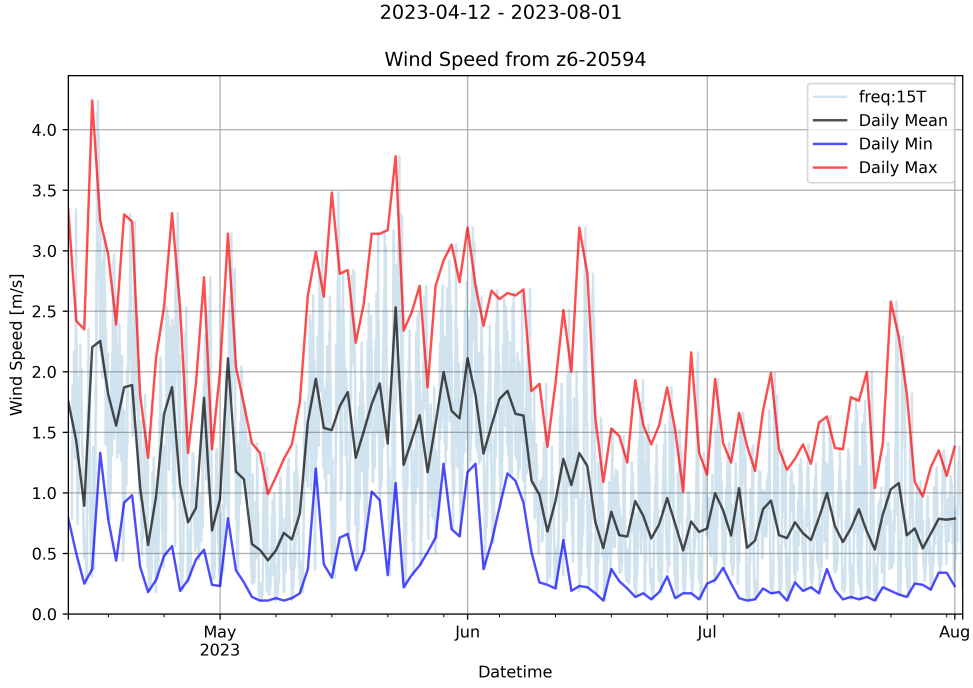


Figure 14: Station Z6-20594 timeseries

Table 11: Values for all variables at the prevailing wind direction at all points in the grid calculation showing mean (\bar{z}_d and \bar{z}_0) and standard deviation (σ_{z_d} and σ_{z_0})

At 340°	\bar{z}_d [m]	σ_{z_d} [m]	\bar{z}_0 [m]	σ_{z_0} [m]
<i>Method</i>				
RT	4.5053	0.7034	0.6436	0.10
MAC	3.0946	0.7282	3.1983	0.65
MHO	9.0454	0.8240	1.3102	0.2688
KAN	5.4060	0.9336	4.0158	0.318
Anemometer		na	0.3535	0.1840

D Extra Results

D.a Exploratory Analysis

2023-01-19 - 2023-08-02

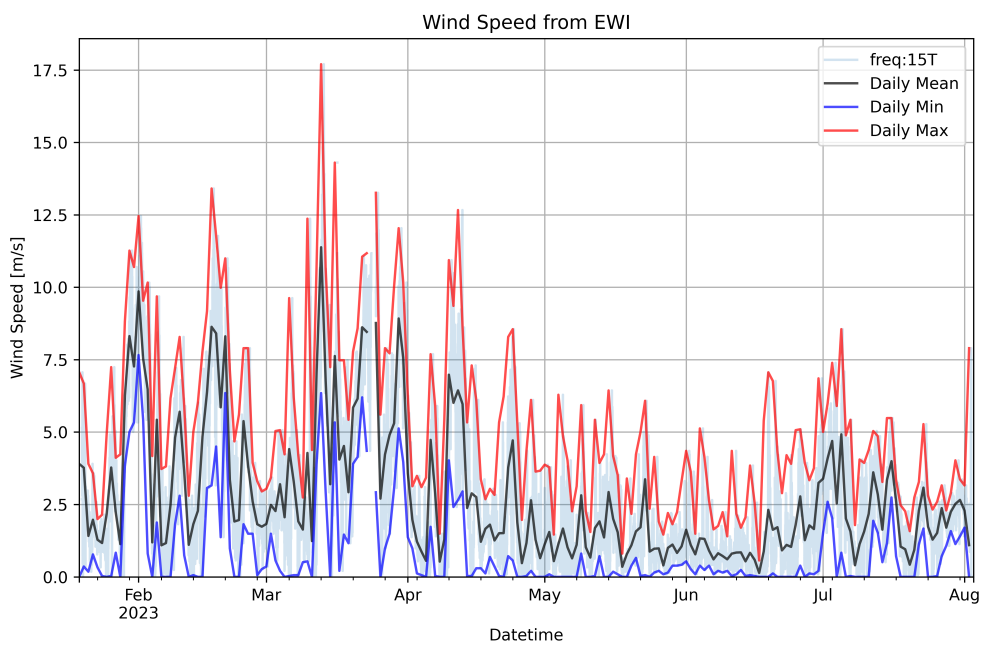


Figure 15: EWI timeseries

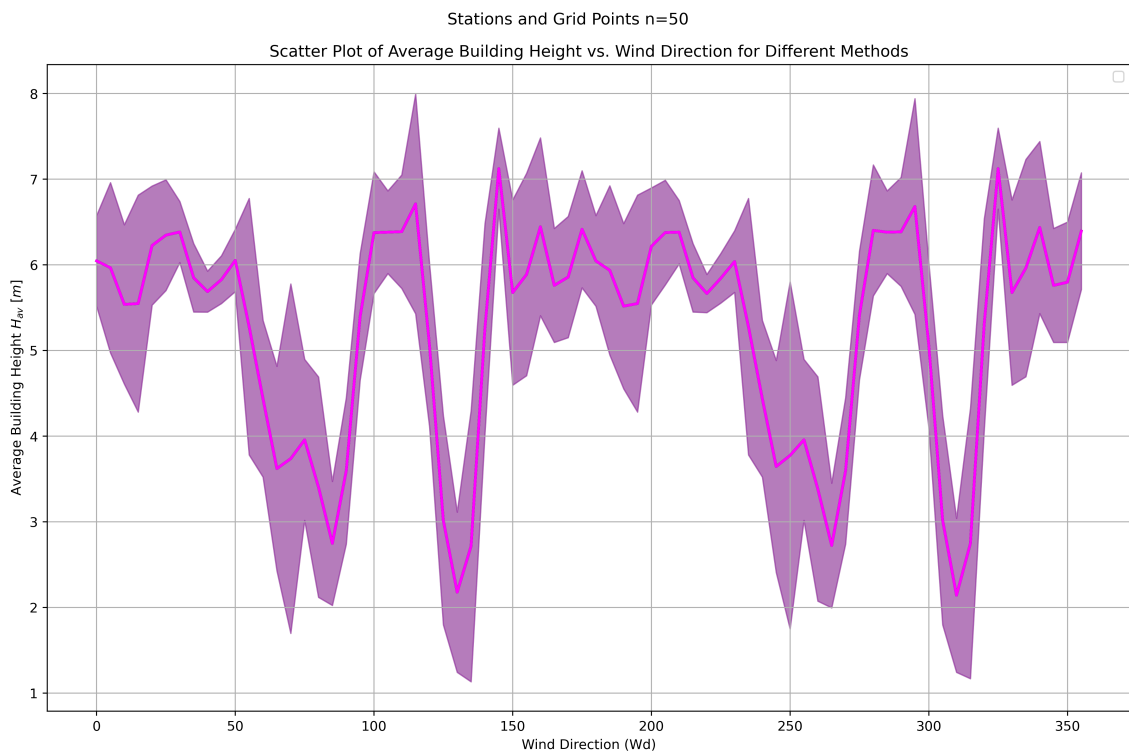


Figure 16: Average building height, ZH , per direction for all grid points. The shaded area is indicative of \pm one standard deviation.

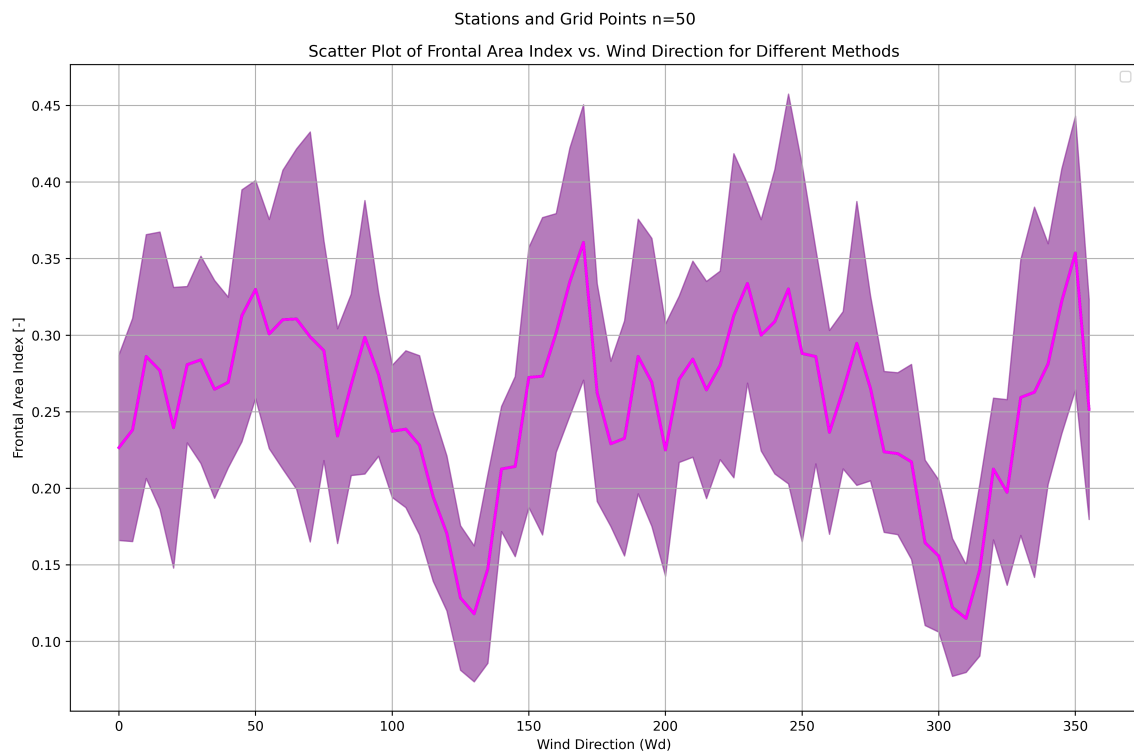


Figure 17: Frontal area index, λ_f , per direction for all grid points. The shaded area is indicative of \pm one standard deviation.

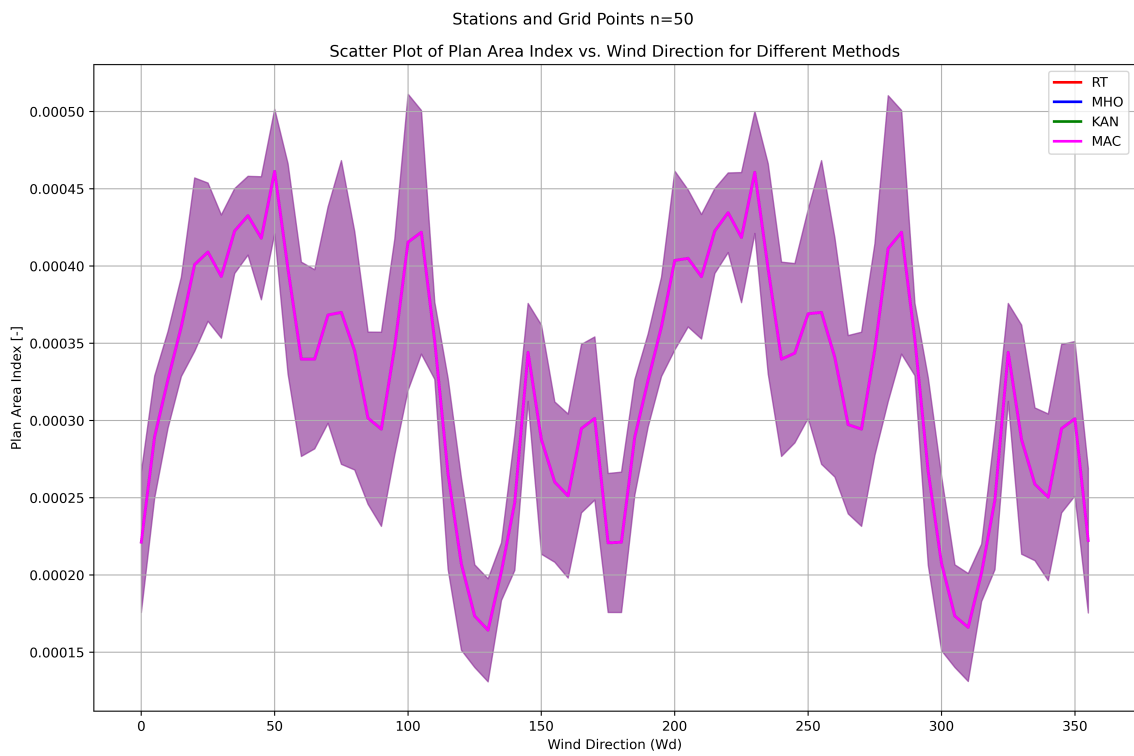


Figure 18: Plan area index, λ_p , per direction for all grid points. The shaded area is indicative of \pm one standard deviation.

References

- Ayub, M., Farooqi, Z. U., Phd, W. U., Nadeem, M., Ahmad, Z., Fatima, H., Iftikhar, I., and Anjum, M. (2021). *Role of Urban Vegetation: Urban Forestry in Micro-Climate Pollution Management*, pages 231–251.
- Barlow, J. F. (2014). Progress in observing and modelling the urban boundary layer. *Urban Climate*, 10:216–240.
- Bruin, H. A. R. D. and Moore, C. J. (1985). Zero-plane displacement and roughness length for tall vegetation, derived from a simple mass conservation hypothesis. *Boundary-Layer Meteorology*, 31:39–49.
- Charnock, H. (1955). Wind stress on a water surface. *Quarterly Journal of the Royal Meteorological Society*, 81(350):639–640.
- Cheng, H. and Castro, I. P. (2002). Near wall flow over urban-like roughness. *Boundary-Layer Meteorology*, 104(2):229–259.
- Christen, A. (2005). *Atmospheric turbulence and surface energy exchange in urban environments: Results from the Basel Urban Boundary Layer Experiment (BUBBLE)*. PhD thesis, Universitat Basel.
- Coceal, O. and Belcher, S. E. (2004). A canopy model of mean winds through urban areas. *Quarterly Journal of the Royal Meteorological Society*, 130(599):1349–1372.
- Delft, T. U. (2023). Ruisdael vm. Online Database. Accessed: 2023-08-01.
- Grimmond, C. S. B. and Oke, T. R. (1999). Aerodynamic properties of urban areas derived from analysis of surface form. *Journal of Applied Meteorology*, 38(9):1262–1292.
- Jiang, L. and O’Neill, B. C. (2017). Global urbanization projections for the shared socioeconomic pathways. *Global Environmental Change*, 42:193–199.
- Kanda, M., Inagaki, A., Miyamoto, T., Gryschka, M., and Raasch, S. (2013). A new aerodynamic parametrization for real urban surfaces. *Boundary-Layer Meteorology*, 148(2):357–377.
- Kent, C. W., Grimmond, S., Barlow, J., Gatey, D., Kotthaus, S., Lindberg, F., and Halios, C. H. (2017). Evaluation of urban local-scale aerodynamic parameters: Implications for the vertical profile of wind speed and for source areas. *Boundary-Layer Meteorology*, 164:183–213.
- Kousis, I., Pigliatile, I., and Pisello, A. L. (2021). Intra-urban microclimate investigation in urban heat island through a novel mobile monitoring system. *Scientific Reports*, 11:9732.
- Lindberg, F., Grimmond, C., Gabey, A., Huang, B., Kent, C. W., Sun, T., Theeuwes, N. E., Järvi, L., Ward, H. C., Capel-Timms, I., Chang, Y., Jonsson, P., Krave, N., Liu, D., Meyer, D., Olofson, K. F. G., Tan, J., Wästberg, D., Xue, L., and Zhang, Z. (2018). Urban multi-scale environmental predictor (umep): An integrated tool for city-based climate services. *Environmental Modelling and Software*, 99:70–87.
- Macdonald, R., Griffiths, R., and Hall, D. (1998). An improved method for the estimation of surface roughness of obstacle arrays. *Atmospheric Environment*, 32(11):1857–1864.

- Millward-Hopkins, J. T., Tomlin, A. S., Ma, L., Ingham, D., and Pourkashanian, M. (2011). Estimating aerodynamic parameters of urban-like surfaces with heterogeneous building heights. *Boundary-Layer Meteorology*, 141(3):443–465.
- Moene, A. F. and van Dam, J. C. (2014). *Transport in the Atmosphere-Vegetation-Soil Continuum*. Cambridge University Press.
- Monin, A. S. and Obukhov, A. M. (1954). Basic laws of turbulent mixing in the surface layer of the atmosphere. *Tr. Akad. Nauk SSSR Geophys. Inst*, 24(151):163–187.
- Nederland, A. H. (2023). Ahn viewer. <https://www.ahn.nl/ahn-viewer>. Accessed: 2023-09-02.
- Oke, T. R. and Cleugh, H. (1987). Urban heat storage derived as energy balance residuals. *Boundary-Layer Meteorology*, 39:233–245.
- Pino, F. (2021a). The green village climate adaptive city. The Green Village Themes. Accessed: 2023-08-01.
- Pino, F. (2021b). The heat square. Accessed: 2023-08-01.
- Roth, M. (2000). Review of atmospheric turbulence over cities. *Quarterly Journal of the Royal Meteorological Society*, 126(564):941–990.
- Shahfahad, Rihan, M., Naikoo, M. W., Ali, M. A., Usmani, T. M., and Rahman, A. (2021). Urban heat island dynamics in response to land-use/land-cover change in the coastal city of mumbai. *Journal of the Indian Society of Remote Sensing*, 49:2227–2247.
- Tennekes, H. (1973). The logarithmic wind profile. *Journal of Atmospheric sciences*, 30(2):234–238.
- Wilson, D. K. (2001). An alternative function for the wind and temperature gradients in unstable surface layers. *Boundary-Layer Meteorology*, 99:151–158.
- Wyngaard, J. C. (2010). *The Atmospheric Boundary Layer*, pages 193–214. Cambridge University Press.
- Wyngaard, J. C. and Coté, O. R. (1971). The budgets of turbulent kinetic energy and temperature variance in the atmospheric surface layer. *Journal of the Atmospheric Sciences*, 28:190–201.
- Ye, X. and Niyogi, D. (2022). Resilience of human settlements to climate change needs the convergence of urban planning and urban climate science. *Computational Urban Science*, 2:6.